Lawrence Berkeley Laboratory
UNIVERSITY OF CALIFORNIA

Physics Division

THE LIFETIME OF THE TAU LEPTON

D.E. Amidei
(Ph.D. Thesis)

May 1984

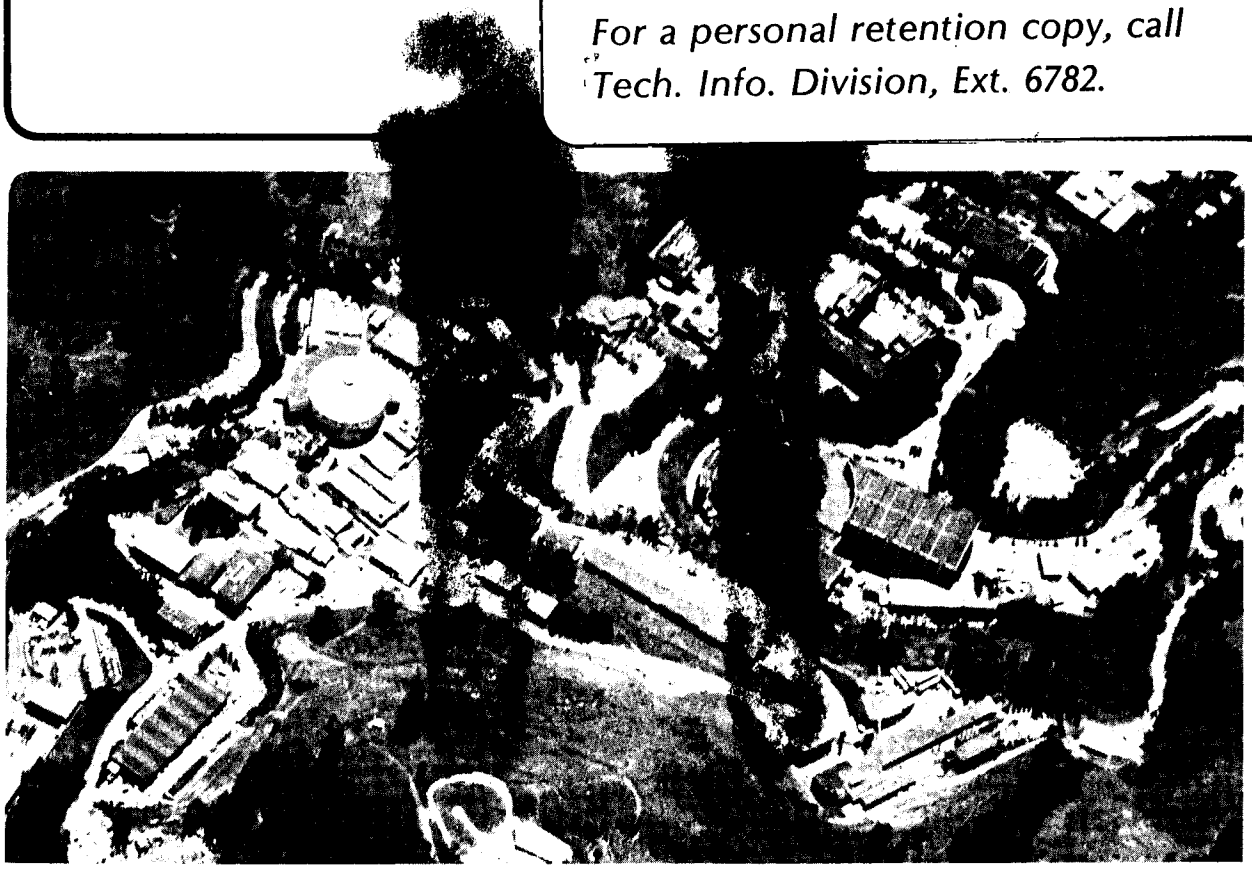

Prepared for the U.S. Department of Energy under Contract DE-AC03-76SF00098

DISCLAIMER

LBL-17795

THE LIFETIME OF THE TAU LEPTON

Dante Eric Amidei

Lawrence Berkeley Laboratory
University of California
Berkeley, California 94720

May 1984

This work was supported by the Director, Office of Energy Research, Office of High Energy and Nuclear Physics Division of High Energy Physics of the U.S. Department of Energy under Contract Number DE-AC03-76SF00098.

The Lifetime of the Tau Lepton

Dante Eric Amidei

ABSTRACT

We have installed a high resolution vertex detector in the Mark II at PEP, and used this detector in a precision measurement of the lifetime of the tau lepton. The result is

$$\tau_\tau = (2.80 \pm .24 \pm 0.25) \times 10^{-13} \text{ seconds}$$

where the first error is statistical, and the second is systematic. This result implies that the tau couples to the charged weak current with an amplitude within 7% of the universal Fermi coupling strength.

George H. Trilling

ACKNOWLEDGEMENTS

Suffice it to say that this measurement would not have happened without the vision and skill of my mentors, John Jaros and George Trilling. Working with these fellows has been a privilege and a pleasure.

More generally, I would like to extend my thanks to the entire Mark II collaboration for all manner of kindness and support.

CONTENTS

1. INTRODUCTION

1.1 The tau lepton

In 1975, the Mark I collaboration at SPEAR discovered anomalous events containing only an electron, a muon, and "missing energy" in the final state resulting from electron positron annihilation [1]. The most straightforward interpretation of these events was the pair production of a new weakly decaying lepton, the tau, with mass of approximately 1.8 Gev/c^2.

Experimental confirmation of this hypothesis quickly followed. The measured threshold behavior of the production cross section was found to be consistent only with the creation of pairs of pointlike spin 1/2 particles [2,3]. Measurement of the Michel ρ parameter in the momentum spectrum of decay electrons was found to favor V-A currents [2]. The measured branching fractions in both leptonic and hadronic channels were quite consistent with theoretical expectations [4]. Finally, all of the above, combined with limits on exotic decay modes and early limits on the lifetime, firmly established the tau as a member of a conventional Weinberg-Salam doublet, with its own neutrino, and its own conserved lepton number [5,27]. The tau then takes its place as a member of a new lepton generation in the Standard Model, a so called "sequential lepton", and will be assumed as such throughout this thesis.

With the identity of this new lepton thus established, it becomes a

new testing ground for the weak interactions. It is particularly appealing in this regard because its leptonic decay channels are free of hadronic complications and, in principle, exactly calculable in the Standard Model. The decay rate to electrons, for instance, can be computed in total analogy to muon decay. The lowest order diagram is shown in fig. 1.1a; the partial width, assuming a massless tau neutrino is

$$\Gamma(\tau\to e\nu_\tau\nu_e) = \frac{g_e^2 g_\tau^2 M_\tau^5}{192\pi^3} \qquad (1.1)$$

$$=\Gamma(\mu\to e\nu_\mu\nu_e)\left[\frac{M_\tau}{M_\mu}\right]^5 \qquad (1.2)$$

The second line assumes that the tau couples to the charged weak current with the same strength as the muon. Higher order corrections are calculable in the Standard Model, they are of order α, and therefore effect the rate only at the 1% level [6].

The utility of this expression is that it is inversely proportional to a very accessible experimental quantity: the tau lifetime. The proportionality factor is the tau branching fraction to electrons. In principle, this branching fraction is calculable, but suffers some uncertainty due to QCD enhancements in the hadronic decay channels. Instead, we can use the experimentally measured branching fraction, $B(\tau\to e\nu_\tau\nu_e) = (17.6\pm1.1)\%$ [4], to find

a)

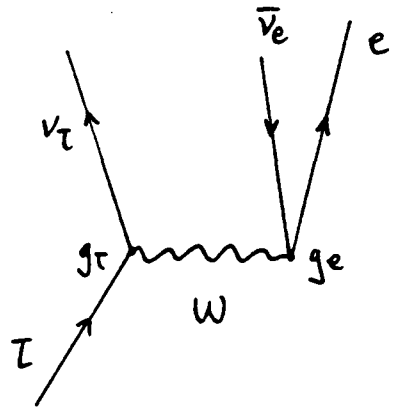

b)

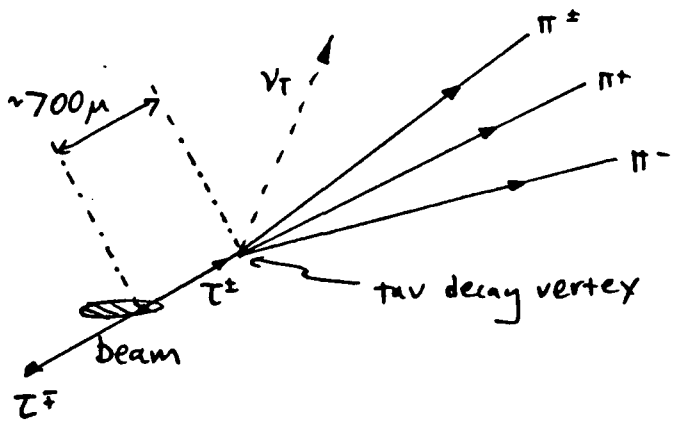

Fig. 1.1 Tau decay
a) lowest order weak decay into electrons
b) in the laboratory

$$\tau_\tau = \frac{B(\tau \to e\nu_\tau\nu_e)}{\Gamma(\tau \to e\nu_\tau\nu_e)}$$

$$= (2.82 \pm 0.18) \times 10^{-13} \text{ sec} \qquad (1.3)$$

This value assumes eqn. 1.2, and uses the Particle Data group value for the tau mass, 1.784 ± 0.003 Gev/c^2. Note that the only major uncertainty in this result is the 6% error associated with the branching fraction.

The ingredients in this rather precise prediction are the fundamental assumptions of the Standard Model:

$M_{\nu\tau} = 0$

no mixing among lepton generations

e-μ-τ universality

I now briefly discuss the way in which a measurement of the tau lifetime tests these assumptions.

A massive tau neutrino increases the lifetime by restricting the amount of available phase space. The dependence on $M\nu_\tau$ is given, to lowest order, by [7]

$$\tau_\tau \to \tau_\tau(1 + 8(M\nu_\tau/M_\tau)^2) \qquad (1.4)$$

The quadratic dependence on $M\nu_\tau/M_\tau$ limits the sensitivity of this measure at small values of $M\nu_\tau$. A recent Mark II measurement has derived a new limit on $M\nu_\tau$ by looking at the endpoint of the four pion mass spectrum in $\tau \to 4\pi\nu_\tau$ [8]. At the 95% confidence level, they conclude

$$M\nu_\tau \leq 164 \text{ Mev}/c^2$$

A tau neutrino mass at the upper limit would give a 7% correction to the lifetime.

If the neutrino is massive, a Cabbibo-like mixing can occur between the neutrinos of the various generations. Since the neutrinos of the known generations are all light compared to the tau, the total decay rate gives no information regarding mixings with the known leptons. In fact, the measured branching rates into exotic final states indicates that if such mixing does exist, it is extremely small [9]. Instead, let us assume that ν_τ mixes with a massive neutrino, N_0, belonging to a fourth lepton generation:

$$\begin{bmatrix} \cos\theta\nu_\tau+\sin\theta N_0 \\ \tau \end{bmatrix} \qquad \begin{bmatrix} \sin\theta\nu_\tau-\cos\theta N_0 \\ N^- \end{bmatrix}$$

If N_0 is more massive that the tau, the total lifetime will be suppressed by a factor of $\cos^2\theta$. In an admittedly model dependent way, the measurement of the tau lifetime can thus probe the existence of new generations.

If we restrict ourselves to three generations and a reasonably massless ν_τ, the real issue addressed by the lifetime measurement is e-μ-τ universality. Simply stated, this is the requirement that each generation of leptons couple with the same strength to the weak bosons. In the Weinberg-Salam model, universality is <u>exact</u>, and follows directly from the requirement that all generations couple to the same gauge bosons [10]. An alternative model has been constructed in which a separate family of gauge bosons and Higgs scalars is postulated for each generation [11]. In this model, universality is an approximate condition arising from the relationship between the vacuum expectation values of the scalars; deviation from universality is expected to be

greatest for the heaviest generation.

More generally, the puzzle of universality seems to echo the more fundamental issue of why multiple generations should exist at all. Many authors have suggested that the explanation of the redundancy lies in some sort of substructure for the known fermions. In several of these models, the weak interaction is seen as a kind of low energy residual of the fundamental force which binds the constituents within the fermions [12]. In this case, the universality of the weak interactions is analogous to the old universal coupling of the vector mesons to the "unitary spin current" [28]. A measured deviation from universality would be an important experimental input to this speculative school of thought.

The most stringent experimental evidence for the e-μ universality comes from a recent high precision measurement of the ratio of pion branching fractions into electrons and muons [13]. Combined with small theoretical uncertainties arising from strong interaction effects and higher order electromagnetic corrections, this measurement implies that the coupling (g_W) of the muon and electron to the charged weak bosons are identical to within a factor of 0.8%. Nothing approaching this kind of precision exists for the tau, although early measurements of the tau lifetime [14], as well as direct measurements of its vector and axial vector couplings [15], are consistent with universality, within rather large errors. One of the goals of this thesis is to make the most precise statement possible with respect to the issue of e-μ-τ uni-

versality.

1.2 Measurement of the tau lifetime in electron-positron annihilation

In addition to the ease of its theoretical description, the tau possesses several attractive experimental features.

The fact that it is copiously pair-produced in electron positron annihilation affords a working environment in which its decays can be studied in isolation. The work to be described here was performed with the Mark II detector at PEP, a colliding electron-positron facility which has operated over the past three years at a center of mass energy of 29 Gev.

The number of charged secondaries from tau decay seldom exceeds three [16]. This low multiplicity reduces the complications of tracking with an electronic detector, and, at PEP energies, helps distinguish tau's from the higher multiplicity hadronic production.

In electron positron annihilation, the tau and its antiparticle are produced monochromatically at the beam energy. Measurement of the lifetime then follows from a measurement of the mean path length:

$$\langle \ell \rangle = \gamma \beta c \tau_\tau \qquad (1.5)$$

To measure the path length, the most straightforward scheme is to use the tau's 3 prong decay mode to form a decay vertex, and measure the distance from this decay vertex to the beam spot. This technique is summarized in fig. 1.1b. It requires the existence of the multiprong mode, a stable measurable beam position, and good tracking resolution

near the origin. The 3 prong mode is a matter of public record [16,17] and I will demonstrate in chapter 3 that beam positions are manageable. But note that formulae 1.3 and 1.5, in conjunction with a beam energy of 14.5 Gev, predict a mean path length of 680 μ. This is a regime which has traditionally been addressed by bubble chambers, or nuclear emulsion, neither of which is yet practical at colliding beam facilities. This makes the issue of tracking resolution at the origin a non-trivial experimental challenge, the details of which are described in the following chapter.

2. EXPERIMENTAL APPARATUS

2.1 The Mark II

The Mark II detector combines charged particle tracking with liquid argon calorimetry and muon identification to provide a general purpose reconstruction of the final states produced in electron-positron annihilation.

The main detector components are summarized in cross section in Fig. 2.1. Although the tau lifetime analysis is almost exclusively dependent on charged tracking alone, I summarize here the main features of the detector for completeness. I begin at the interaction point (IP) and move radially outward.

Closest to the interaction point is the secondary vertex detector. The vertex detector is a high resolution drift chamber designed to give the greatest possible precision in tracking and vertexing close to the origin. As this detector is indispensable to this thesis, it will be described in some detail in the next section.

Surrounding the vertex detector is the larger main drift chamber (DC) [18]. This chamber contains 16 equally spaced concentric layers of drift cells, covering radii between 41 and 145 cm. In six of these layers, the sense wires are axial; in the remainder, the sense wires are canted at $\pm 3^0$ to provide stereo information. All layers are enclosed in a common gas volume, which is filled with a 50/50 mixture of argon ethane at ambient pressure. The resolution per layer is

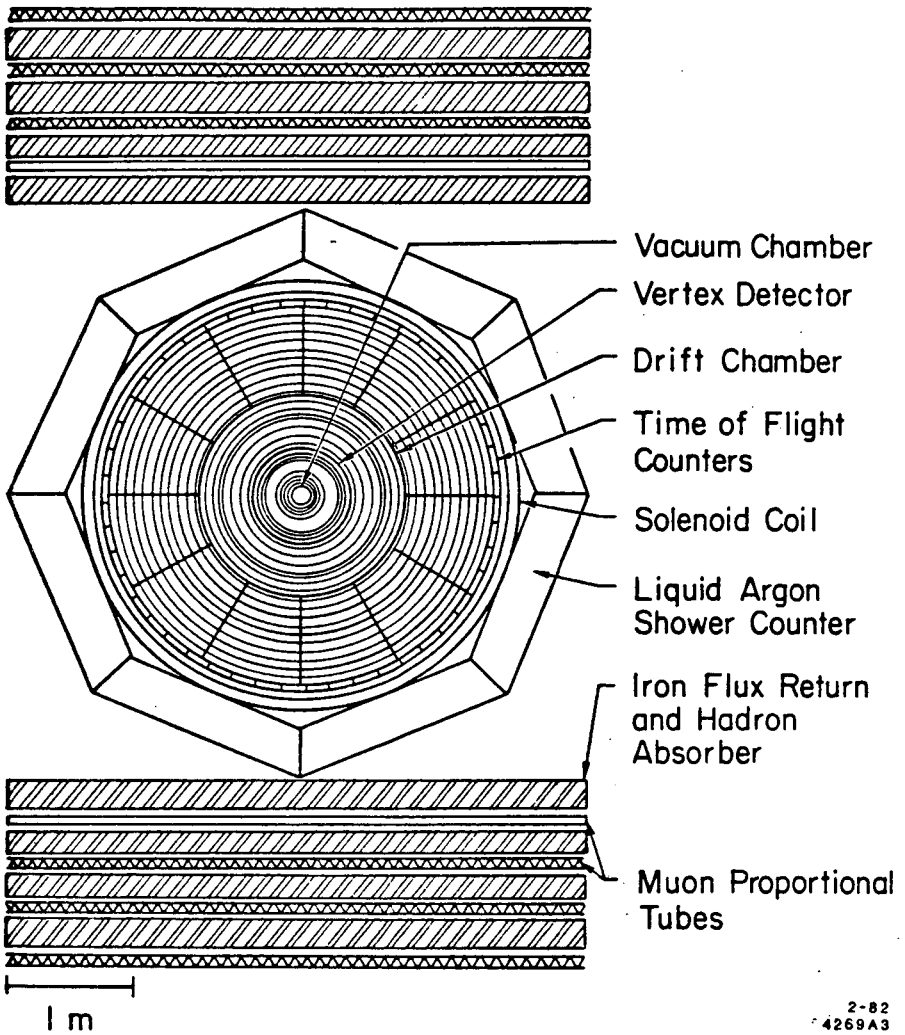

Fig. 2.1 The Mark II detector. The muon walls on the sides are not shown.

approximately 200μ. As the entire chamber is encased in a large solenoid, track curvature allows the measurement of momentum. The rms resolution in the plane perpendicular to the beam is

$$\frac{\delta p_\perp}{p_\perp} = \sqrt{(.02)^2 + (.011 p_\perp)^2}$$

where the first contribution is from multiple coulomb scattering, and the second is from the inherent position resolution of the chamber.

Lying next to the outer shell of the drift chamber, at a distance of 1.51 m from the IP, are 48 longitudinal strips of Pilot F scintillator. These strips are read out by photomultipliers at each end, and measure particle flight times with an accuracy of about 400 psec. During the tenure of the Mark II at SPEAR, this system provided particle identification; in the high energy regime at PEP, however, it is relegated mainly to providing trigger information and rejecting cosmic rays.

All of the components described thus far are enclosed in a solenoidal coil of radius 1.6 m. The coil consists of two water cooled aluminum conductors, and comprises about 1.4 radiation lengths. For the majority of the data used in this thesis, only one conductor was powered, providing an axial magnetic field of 2.3 kG. The flux return is via two steel doors which close over the ends of the coil and are connected by steel slabs which run over the top and bottom of the detector. The entire field volume was mapped out before installation with a Hall probe; NMR probes mounted near the beam pipe at each end provide a reference for carrying this initial map forward to the present. Within

the tracking volume, the field is uniform to within half a percent.

Eight liquid argon sampling calorimeter modules are mounted octagonally outside of the coil [19,20]. Each module contains 37 layers of 2 mm lead planes alternated with 3 mm liquid argon gaps. The lead doubles as both shower and readout medium. The lead planes are subdivided into narrow ($\simeq$ 4 cm) strips; orientation of the planes in three different directions creates a cross hatching of strips which provides shower localization. To minimize electronics cost, the 37 layers are ganged to provide six samples in depth. The entire system is 14 radiation lengths deep, and covers about 65% of the solid angle. The energy resolution of the system is $15\%/\sqrt{E}$; the spatial resolution is such that a Bhaba electron is localized to within 7mm of its entry point.

Outside of the shower counters is a system for detecting penetrating muons. Four muon "walls" surround the detector azimuthally, covering about 45% of the solid angle. Each wall is a four layer sandwich of proportional tubes and iron. The iron in the top and bottom walls doubles as the flux return for the magnet.

In addition to the "radial" coverage just outlined, a limited effort has been made to instrument the ends of the detector. Lead proportional wire chamber modules mounted on the steel end doors provide electron and photon identification in the polar angular region from 15^0 to 40^0. Unfortunately the energy resolution of this system is a rather marginal $50\%/\sqrt{E}$, and, like the time of flight system, its usefulness is restricted mainly to providing trigger information. Finally, in the

"small angle" region between 21 and 82 mrad in polar angle, lies a combination of drift chambers, lead scintillator shower counters, and acceptance defining scintillators. This system is designed to identify high energy electrons resulting from two photon processes and low q^2 Bhaba scattering. The small angle Bhaba rate also provides an online measure of luminosity [21].

The coordination of these sundry systems into a functional unit occurs through a hardware trigger. The high beam crossing rate at storage rings (400 kHz at PEP) necessitates a two-tiered system. A fast primary trigger checks for simple multiplicity and threshold requirements at each beam crossing. The charged primary trigger, for instance, requires hits in at least 9 drift chamber layers spread between the inner and outer radii. Other primary triggers recognize summed neutral energy in the calorimeters, or collinear bhaba candidates in the small angle system.

If the primary requirements are met, further data collection is halted, and processing moves to the next tier. This secondary trigger consists of 24 microprocessors which work in parallel to identify charged track candidates in the drift chambers and time of flight system. Requirements on these candidates then comprise the secondary trigger logic. The charged secondary, for instance, requires 2 hardware tracks with a minimum radius of curvature of 1.7 m ($p_\perp \geq$ 130 Mev/c) within the central 75% of the solid angle. If the secondary requirements are met, the detector electronics are read out by computer and

transferred to magnetic tape. Typical secondary trigger rates at PEP were 1 to 2 Hz.

2.2 The Mark II Vertex Detector

2.2.1 Introduction

A tau of canonical lifetime will travel less than 1 mm before decaying. The precision of a mean path length measurement thus depends critically on obtaining reliable tracking information from as close to the origin as possible. To this end, the "original" Mark II was augmented, in the summer of 1981, with a high precision tracking chamber located between the beam pipe and the main drift chamber. This inner detector was optimized for the reconstruction of secondary vertices, hence the appellation vertex detector or vertex chamber (VC). In addition to enabling the study of the tau discussed here, the VC has had great success in the measurement of heavy quark lifetimes [22,23]. The extra tracking information near the origin has found obvious utility in the primary and secondary triggers, as well as improving the overall momentum resolution of the entire detector.

The vertex detector is shown in side view in fig 2.2. It is a cylindrical drift chamber, 1.2 m long, and 0.70 m in diameter. All wires are strung axially between two 5 cm aluminum endplates. The outer shell is also aluminum, 0.18 cm in thickness, and completely supports the wire tension load on the endplates. The inner shell is the beam pipe itself. In order to motivate a discussion of the detailed

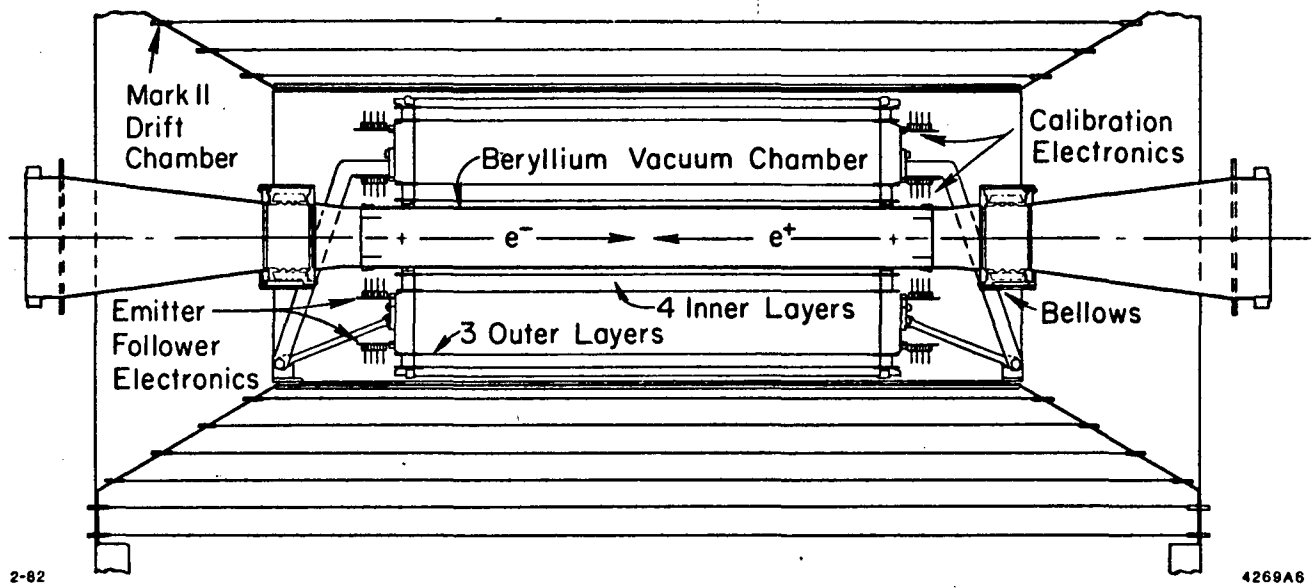

Fig. 2.2 The Mark II vertex detector

features of this detector, I digress briefly to a simple parameterization of the requirements of "precision".

Consider the accuracy with which a single track can be extrapolated to the origin, and let the rms miss distance be σ_{miss}. One kind of contribution to σ_{miss} arises purely from the interpolation of a fit to data points with finite errors. Here, the data points are drift time measurements, and their errors are usually referred to as the "resolution per layer", σ_r. The scale of σ_r is set by mechanical and electrical tolerances, as well as the inherent limits imposed by ionization statistics and diffusion. For a straight line fit to N layers at radii r_i, with constant resolution σ_r at each layer, the extrapolated error at the origin can be shown to be

$$\sigma_{ex} = \sigma_r \sqrt{\frac{\Sigma r_i^2}{N \Sigma r_i^2 - (\Sigma r_i)^2}} \qquad (2.1)$$

Another kind of contribution to σ_{miss} arises from the angular uncertainty borne of multiple coulomb scattering. The main offender here is the material between the origin and the first drift time measurement; it was in order to minimize the amount of this material that the beam pipe was chosen to double as the inner gas seal. For a pipe of radius r_b, t radiation lengths in thickness, the multiple coulomb contribution to the miss distance can be written as

$$\sigma_{MCS} \cong \theta_{MCS} r_b \cong \frac{.015}{p\beta} \sqrt{t}\, r_b \qquad (2.2)$$

The mean error at the origin is then expected to be something like

$$\sigma_{miss}^2 = \sigma_{ex}^2 + \sigma_{MCS}^2 \qquad (2.3)$$

The design and construction of the vertex chamber was carried out with the minimization of σ_{miss} as its goal.

2.2.2 Beam pipe

The design of the beam pipe is almost entirely constrained by the requirement of minimal σ_{mcs} and the realities of a colliding e^+e^- machine [24].

To start, eqn 2.2 indicates that r_b should be as small as possible. To set the lower limit, note that the interaction region at PEP is bathed in an envelope of synchrotron radiation produced at the final focusing quadropole. This radiation is an unhealthy background for wire chambers; it produces excessive ionization, leading to high chamber currents which can compromise performance. It follows that this envelope must be completely contained within the beam pipe; to accommodate it safely, we put

$$r_b = 7.8 \text{ cm.}$$

Eqn. 2.2 now indicates that the thickness in radiation lengths should also be minimized. We clearly want a low Z material, and beryllium, with Z=4, is an obvious choice. The actual mechanical thickness now follows from the pressure differential across the pipe, and the safety requirement that it withstand four times this amount. The VC

was designed to operate at two atmospheres and the interior of the PEP beam pipe is at vacuum. For cylindrical Be, the ASME boiler code then sets the pipe thickness at 1.42 mm.

The design which then emerges is a beryllium tube, 1.4 m long, 15.6 cm in diameter, and 1.42 mm thick. Each end is brazed to an aluminum stainless steel transition piece, which in turn is welded to a stainless steel bellows. The bellows are attached to the PEP beam pipes; they serve to reduce stresses from misalignment and thermal expansion.

In order to isolate the chamber ground from the PEP ring, the outside of the pipe is covered with a 50 μ mylar sheet, and this sheet is covered with a layer of 25 μ aluminum foil. The foil is electrically connected to the aluminum endplates, completing the chamber shield.

One further embellishment is motivated by the presence of thick lead masks at ± 3 m from the interaction point. Calculation showed that some synchrotron radiation could backscatter from these masks and enter the chamber at small angles. To protect against this possibility, the inside of the beam pipe was lined with a 50 μ titanium foil, attached to the beryllium with a seam weld at each end. Although quite thin at normal incidence, this lining suffices to absorb the backscattered photons at grazing incidence, while florescing with a spectrum that can be absorbed by the beryllium.

The complete beam pipe amounts to 0.6% of a radiation length at normal incidence.

2.2.3 Wire positioning

To minimize the extrapolation error, we want to place sense wires as close as possible to the beam pipe. To maximize the accuracy of the track angle measurement, we also want to place sense wires as close as possible to the outer shell. These choices minimize the numerator and maximize the denominator of eqn 2.1. Obviously, we would like to have as many layers as possible in between, but this desire is tempered by the finite amount of space available on the endplates for the associated instrumentation. Our compromise solution is to place four layers close to the pipe, three layers close to the outer can, and use the intervening space on the endplates for cabling and electronics.

A well understood spacetime relation is a necessity for good resolution; the VC wire array is designed to keep this relation simple. This will be discussed in detail somewhat later. The array is formed from two kinds of layers arranged in an alternating concentric sequence: one kind, called a 'field layer' contains only cathode wires, while the other, a 'sense/field' layer, alternates sense and cathode wires. The pattern is completely specified by two constants: the distance between layers, which is set to 0.422 cm, and the arclength between wires in a layer, which is set to 0.530 cm The result for the four layer inner band is shown in fig. 2.3a. The pattern conspires to produce roughly rectangular drift cells. Sense wires are thus electrically isolated from their neighbors, and cross talk is minimized. The outer band of three layers is similar. The inner and outer bands contain 270 and 555

a)

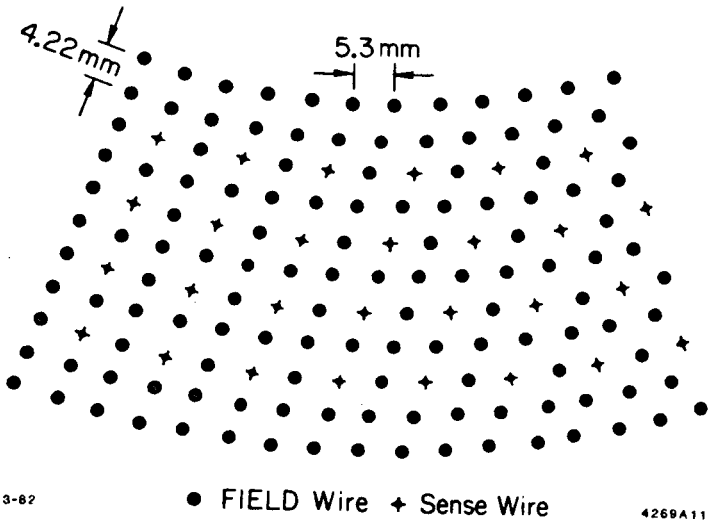

b)

	Layer No.	Radius (cm)	No. of Sense Wires
Inner Band	1	10.1223	60
	2	10.9658	65
	3	11.8093	70
	4	12.6528	75
Outer Band	5	30.3668	180
	6	31.2103	185
	7	32.0538	190

Fig. 2.3 a) The VC wire array
b) Sense wire placement in the VC

sense wires respectively;. The radii of the seven sense layers are given in fig. 2.3b.

The sense wires are at ground, and the cathode wires run at a common negative high voltage. Fig. 2.3a shows an extra field layer at both edges. These "guard layers" are used to compensate for edge effects; an appropriate (somewhat lower) choice of high voltage balances the gains on the sense layers, while simultaneously minimizing electrostatic deflections at the borders.

Wires are positioned individually with nylon feedthroughs, as shown in fig. 2.4a. The aluminum endplates were precision machined with a tapered hole for each wire. The feedthroughs were injection molded with a corresponding taper, and a 225 μ positioning hole concentric to the taper. The vagaries of the injection molding process actually caused the hole position to wander off center up to 100 μ. We used a high power microscope to sort the feedthroughs according to hole position, and used the most accurate ones for the sense wires. The accuracy of sense wire location affects the chamber performance through σ_r of eqn 2.1. We believe the above technique positions our sense wires with an rms error of approximately 15 μ.

The sense wires are 20 μ gold plated tungsten and were strung at a tension of 50 g. The maximum wire sag is calculated to be 25μ at the center of the chamber; corrections for sag are included in the tracking program. Cathode wires in the outer band are 150 μ gold plated copper-beryllium. To further minimize the effects of multiple coulomb

a)

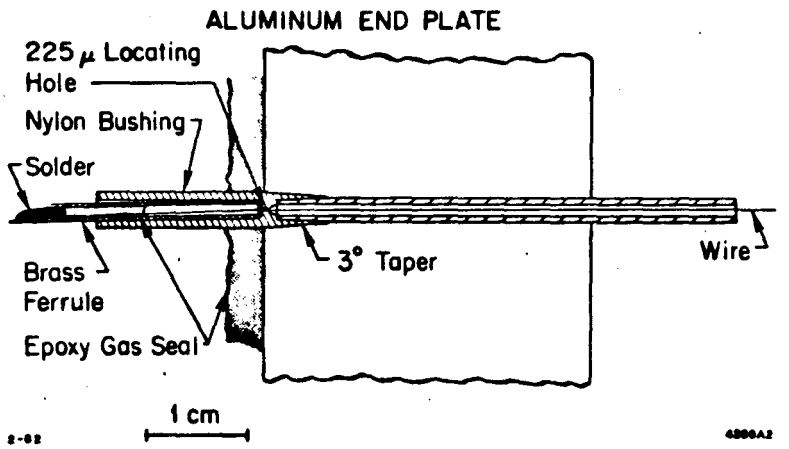

b)

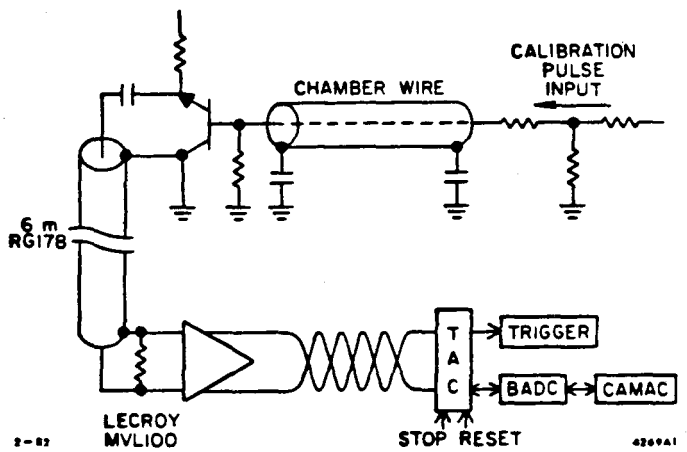

Fig. 2.4 a) The VC feedthrough
b) VC calibration and readout electronics

scattering, 150 μ gold plated aluminum was used for cathode wires in the inner band. All cathode wires were strung at a tension of 200 g.

2.2.4 Electronics

The last ingredient in the quest for high resolution (small σ_r) is good electronics. The VC scheme is shown in fig. 2.6. One end of the chamber carries the readout, and the other end carries high voltage and calibration input.

For readout, the chamber pulse is coupled to 6m of 50Ω coaxial cable through a fast emitter-follower. The emitter-followers serve only to match impedances, and are mounted directly on the aluminum endplate, as shown in fig. 2.2. The coaxial cables run to a shielded preamp box containing 825 channels of Lecroy Research Systems model 7791 16 channel amplifier/discriminators. The rise time of these amplifiers is 5 ns. The discriminators drive 17 m of twisted pair which ferries the signal to the Mark II electronics house. Each channel is supplied with a time to amplitude converter (TAC) which measures the time between chamber pulse and a common stop. The TACs are read out by a dedicated microprocessor (BADC) which corrects for channel to channel timing offsets and gains. If the secondary trigger information is satisfied, the information is transferred via CAMAC to a VAX 11/780 computer which writes the data to tape. The accuracy of the TAC/BADC combination is 250 psec throughout the entire system.

The electronics is calibrated by providing a common start time to

the entire array from the other end of the chamber; the arrival times of these signals at the TACs then provides a measure of the channel to channel offsets already mentioned. The start pulse is fanned to all channels simultaneously within about 350 psec. To avoid channel to channel coupling, we actually carry out two sequential calibrations in such a manner that adjacent channels are calibrated separately. During data taking, this calibration procedure is implemented once every eight hour shift.

2.2.5 Operation

The vertex detector runs with a 50/50 mixture of argon ethane. In order to stabilize the gain, the gas pressure is held constant at 15.50±.05 psia.

Fig. 2.7 shows the efficiency as a function of high voltage for the inner four layers with our standard discriminator setting of 400 μV. The fact that all four layers are the same, within errors, indicates that the guard wire scheme has succeeded in balancing gains. The chamber is fully efficient above 2.050 KV; the plateau does not go exactly to 1.0 because of tracking errors. High gain increases resolution by minimizing the effects of slewing in the preamps; our standard running point is therefore somewhat above the knee, at 2.25 KV. As will be discussed in the next chapter, the resolution which results is approximately 100μ per layer.

With all major chamber parameters now in hand, it is interesting

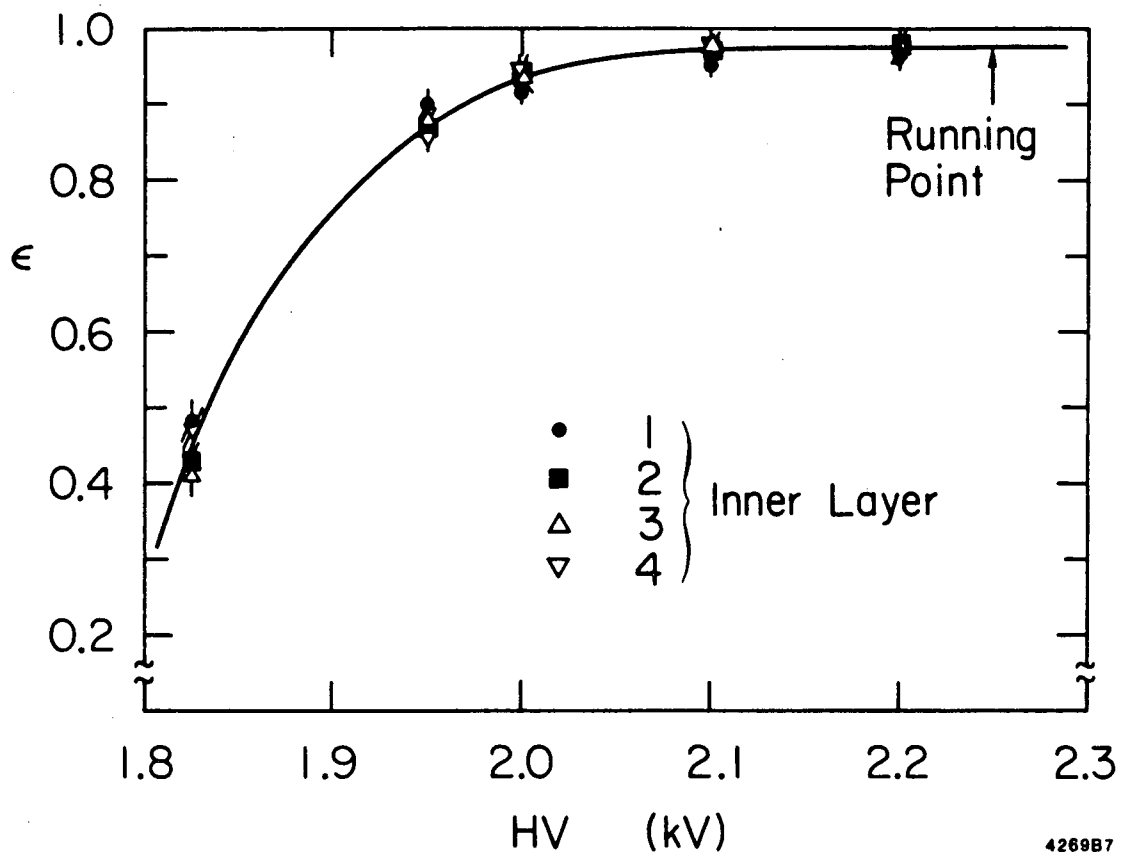

Fig. 2.5 Vertex detector efficiency in inner four layers

to return to eqns 2.1-2.3 and ask what kind of precision we expect from this detector. Using σ_r as above, layer radii as per fig. 2.4, and beam pipe parameters as per section 2.2.2, we find

$$(\sigma_{miss})^2=(85)^2 + (95/p)^2 \ \mu^2$$

For a 14.5 Gev/c bhaba, this predicts $\sigma_{miss}\simeq 85\ \mu$, an impressive expectation. The degree to which this is fulfilled will arise as a kind of recurring motif in the rest of this work.

3. EVENT RECONSTRUCTION

3.1 Introduction

Before the appearance of useful physics results, the list of wire numbers and drift times returned by the tracking chambers must be manipulated into a reconstruction of track orbits. Relevant details to this process include the tracking algorithm, the treatment of multiple scattering errors,the geometrical relation between the VC and the main drift chamber, and the VC space-time relation and resolution. As accurate tracking is crucial to the tau lifetime analysis, I shall briefly discuss each of these items. Following this, I shall also include descriptions of some other pertinent offline items: the determination of beam positions, and some checks on VC performance.

3.2 Tracking

Track reconstitution begins with a pattern recognition algorithm which associates drift points to a single track and resolves left right ambiguities. A χ^2 minimization technique is then used to fit a helical orbit to the chosen points [18]. The five helix parameters used in this algorithm are the azimuth (ϕ), the tangent of the dip angle ($\tan\lambda$), the curvature ($1/p\cos\lambda$), the distance of closest approach to the origin in the equatorial plane (ξ), and the distance of closest approach along the beam line (η). In the version of the algorithm that treats the VC and DC as a combined system, an additional parameter allows for a kink due to multiple coulomb scattering at the interface

between the two chambers.

Let the track parameters be represented by α_μ. The distance of closest approach of a fitted track to the ith wire is some function of these α_μ's, $d^i_{fit}(\alpha_\mu)$. Let d^i_{time} be the distance of closest approach to this wire as measured by the drift time and the space-time relation. For a resolution σ_i, the χ^2 of the track fit can be written as

$$\chi^2_z = \sum_{i=1}^{n} \frac{(d^i_{fit}(\alpha_\mu)-d^i_{time})^2}{\sigma_i^2} \qquad (3.1)$$

where n is the total number of hits associated with the track. Minimization yields the optimal track parameters and their associated error matrix.

The magnitude of the tracking errors is increased by multiple coulomb scattering. The calculation of this effect has two parts. One considers the contribution of gas and wires in the region between the innermost layer of the VC and the outermost layer of the DC. The other calculates explicitly the contribution of the beam pipe and the material between the VC and DC. (The exact treatment of the latter effect obviously depends on whether or not a kink has been fitted at the boundary.) In both cases, the detector materials are parameterized in terms of effective radiation lengths, and average corrections are made additively to the elements of the track error matrix.

A global track fit which treats the VC and DC as one large system is sensitive to the possibility of small geometric misalignments between

the two chambers. A tracking program called ADDTC was developed to allow for this contingency [29]. The program first fits the track in the DC alone, yielding $\alpha_{\mu dc}$ and χ^2_{dc}. A refit with the inclusion of the VC information then treats χ^2_{dc} as the implicit summary of the DC information:

$$\chi^2_z = \sum_{VC} \frac{(d^i_{fit}(\alpha_\mu)-d^i_{time})^2}{\sigma_i^2} + \chi^2_{dc} \qquad (3.2)$$

The change in χ^2_{dc} due to small changes in the α's resulting from the refit can be written as

$$\chi^2_{dc'} = \chi^2_0 + \sum_\mu \sum_\nu (\alpha^\mu-\alpha^\mu_0)\, A_{\mu\nu}\, (\alpha^\nu-\alpha^\nu_0) \qquad (3.3)$$

where χ^2_0 and α_0 are quantities from the initial DC fit, and $A_{\mu\nu}$ is the inverse of the error matrix associated with the α_{dc}'s.

The advantage of expressing the χ^2 in this way is that it allows arbitrary modifications to the weight of selected parts of the DC information. We are counting on the VC to supply high quality information about the azimuth and x-y location of the track; we worry about contaminating this information with geometrical aberrations in the DC, or in the relation between VC and DC coordinate systems. This uncertainty is easily handled in the above formalism by adding extra contributions $(\delta\phi)^2$ and $(\delta\xi)^2$ to the appropriate matrix elements in eqn 3.3.

Note that the effect of taking $\delta\phi$ and $\delta\xi$ very large is equivalent to decoupling the chambers; in this case, the DC supplies the curvature

and z information, and the VC supplies the angular and positional information. Although this weighting is least sensitive to the relevant geometrical quirks, it has the disadvantage of excluding the VC information from the curvature measurement. The "optimal" choice of the uncertainties, found from a study of track χ^2, is

$$\delta\xi = 200\mu$$
$$\delta\phi = 0.3 \text{ mr}$$

All track fitting used in the tau analysis utilized this technique.

3.3 Vertex detector constants

Incorporation of the vertex detector into the track fitting schema requires a knowledge of the space-time relation (STR) for the chamber, as well as of the geometric relationship between the VC and DC. Both sets of constants were found by an iterative χ^2 technique; our procedure was to use a crude estimate of the STR to find the geometry, then use the new geometric constants to find a better estimate of the STR, and so on. In practice, this process converged quite rapidly, consistent with the expected lack of correlation between these two quantities. All constant finding used isolated high momentum tracks to reduce complications from tracking errors.

For finding the geometric constants, we treated the VC and DC as rigid bodies with attached coordinate systems related by displacements in x and y, and small Euclidean rotations around x, y, and z. After deriving the dependence of the tracking residuals on these parameters, a χ^2 like the one of eqn. 3.1 was used to get the best estimate. Fur-

ther details of this calculation are outlined in Appendix A.

The statistical error on the displacements was typically 5 to 10 μ. The constants were recalculated after every access or earthquake and stored in a run dependent data base. They are used to transform the VC wire positions into the DC coordinate system at the commencement of analysis on each event.

The elucidation of the space-time relation was facilitated by several features of the VC wire array. The fact that the drift cell is closed on all sides means that the electric fields therein are mostly radial. This minimizes the dependence of the STR on track angle. In fact, the proximity of the chamber to the IP means that most tracks depart only slightly from radiality, anyway. This presents another advantage. Although the shape of the drift cell varies from rectangular to hexagonal as the pattern sweeps through phi, the radiality of the tracks implies that the first ionization cluster tends to come from somewhere between the sense wire and the adjacent field wire <u>in that layer</u>. The STR then depends mainly on just the sense/field wire spacing. Since this spacing is constant throughout the array, we can use one space-time relation for the entire chamber. Finally, the small drift distance keeps the STR very close to linear.

With all of the above in mind, our parameterization of the STR is a simple cubic in the drift time:

$$D=a_0+a_1T+a_2T^2+a_3T^3$$

The track χ^2 depends on the a_i's purely through the d_{tim} term.

Using an estimate of σ_i in the VC, minimization gives a new estimate of the a_i's; the tracks are refit with these constants and the process is repeated until convergence.

The resultant STR is shown in fig. 3.1. It is nicely linear over most of the drift length. The statistical error on the constant term is typically about 10μ. Long term variation in the constants was basically confined to a_0, which responds to drift in the overall timing of the detector electronics. Attempts to discern extra non-linear correction factors in the regions near and far from the sense wire yielded no significant improvement in resolution.

3.4 Vertex detector resolution

The VC resolution per layer is the ultimate measure of our success at high precision chamber building. In addition, the VC resolution will be a major component of the calculated path length error in the lifetime analysis. As the measured lifetime is rather sensitive to assumed magnitude of this error, the correctness of the assumed chamber resolution merits rather careful attention.

A preliminary measure of the resolution follows from the distribution of tracking residuals in the chamber. As seen in fig. 3.2, this distribution is nicely gaussian; its width is 83 μ. This figure is actually better than the resolution, since each residual is, itself, included in the fit.

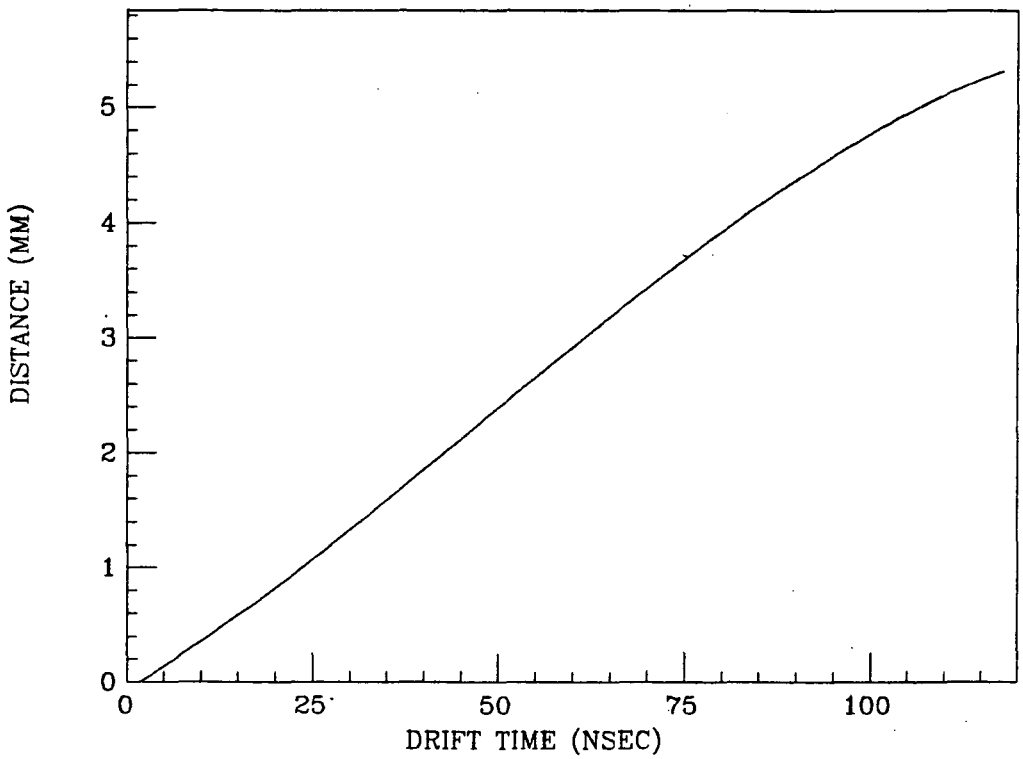

Fig. 3.1 The VC space time relation

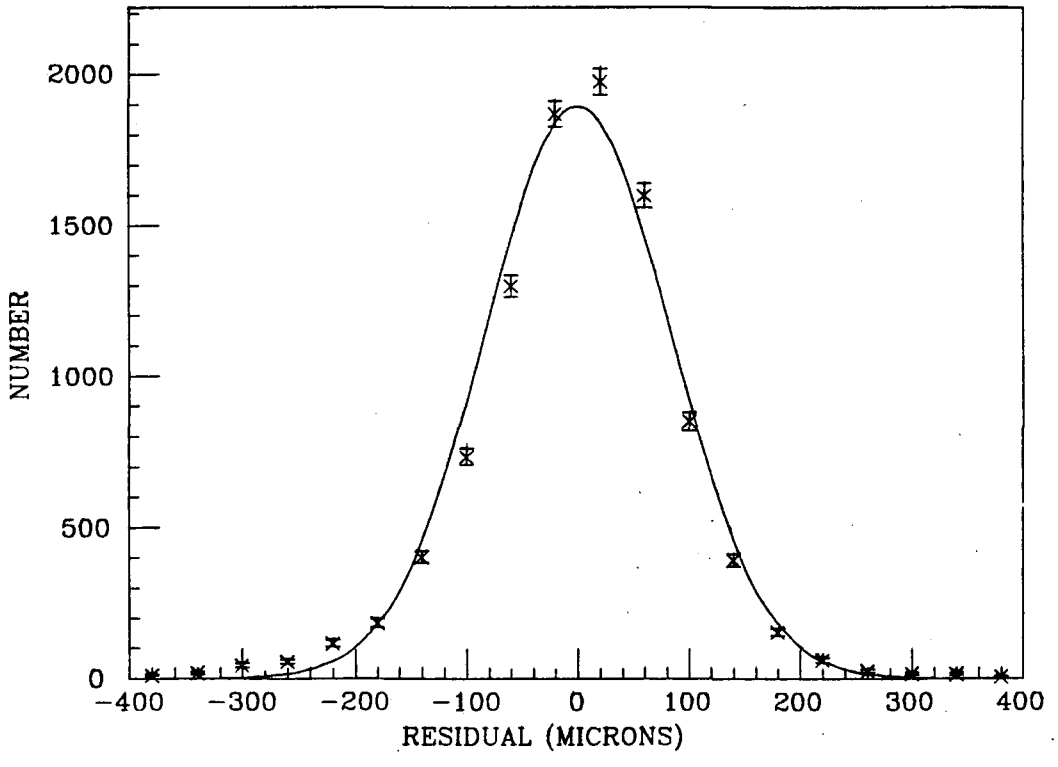

Fig. 3.2 VC tracking residuals

A more sophisticated estimate follows from an analysis of the contribution of the VC to the track χ^2. In the limit of gaussian errors, the χ^2 distribution is exactly calculable, and is a comprehensive measure of all assumptions involved in the fit. We can therefore measure the resolution as that value which gives the best fit to the expected χ^2 distribution.

Since the track is actually fit through both the VC and DC, there is some question about what the χ^2 in the VC alone really means. With the ADDTC algorithm described above, we can imagine that the VC information is basically being used to find the two quantities ξ and ϕ. If we limit the sample to tracks which have hits in all seven VC layers, we can think of the VC χ^2 as that expected for 7-2=5 degrees of freedom. Fitting the distribution of residuals from 7 hit tracks to the shape expected for a χ^2 with 5 degrees of freedom yields a mean resolution per layer of 95±10 μ. The concomitant χ^2 distribution, shown in fig. 3.3, indicates a good fit.

3.5 Beam positions

As per the discussion of sec. 1.2, the position of the luminous region is a necessary ingredient in the determination of the tau path length. We have determined the beam position by two independent techniques and verified that they cross check. The nearness of the VC layers to the IP naturally enhances the effectiveness of both methods.

One technique looks for the average intersection point of bhabas

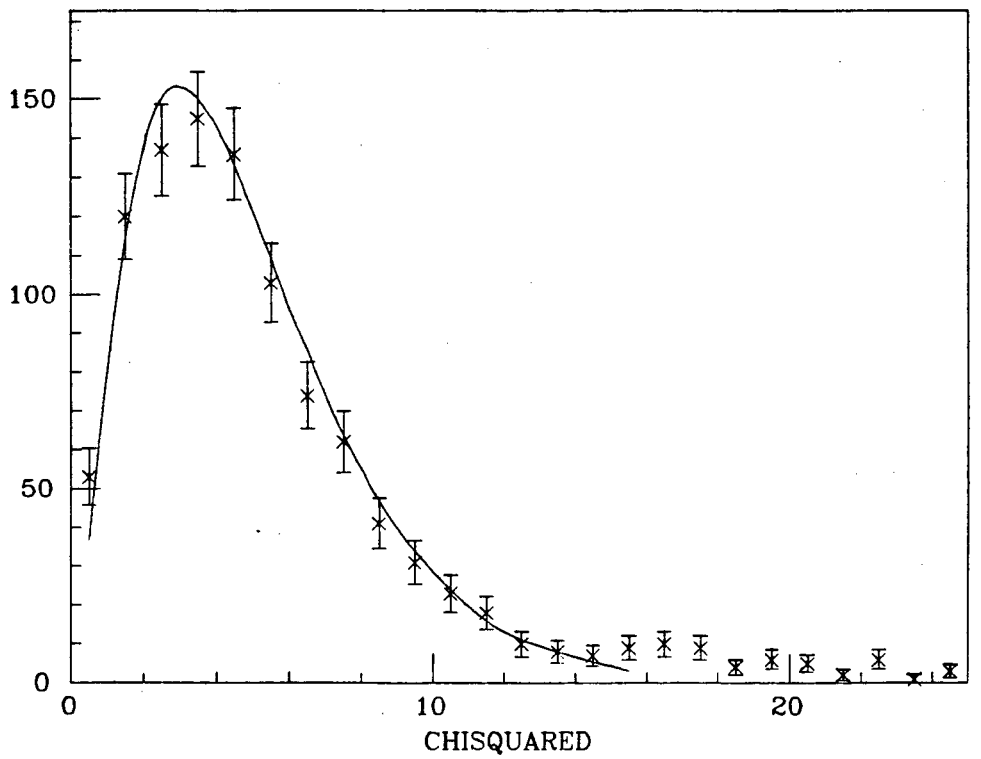

Fig. 3.3 Single track χ^2 in the VC

taken from blocks of 10 to 20 runs. Tracks in a narrow swath around $\phi=\pi/2$ will determine the x coordinate of the beam (x_b), and tracks in a narrow swath around $\phi=0$ will determine the y coordinate (y_b). Corrections are applied for the finite angular extent of the swath. To enhance statistics, the total azimuth is actually divided into several sets of such orthogonal swaths, and (x_b,y_b) is found in the coordinate system defined by each set. All values are then rotated back into the DC coordinate system and averaged. The statistical error on x_b and y_b for each block of runs is about 15 μ. The systematic offset is estimated to be less than 20 μ. I shall refer to beam positions found in this way by their Mark II software name: XYZIR.

The large number of runs required to achieve a decent statistic leaves the XYZIR technique vulnerable to the beam steering that sometimes occurs between storage ring fills. Larry Gladney therefore developed a program called ORCALC which is capable of finding the beam position on a run by run basis. This method uses all good tracks in a run, and calculates the (x_b,y_b) which minimizes the distance of closest approach (DCA) for the entire ensemble. In a typical 2 hour fill, the average beam position is measured with an accuracy of 50 μ horizontally and 20μ vertically. Since the spread in DCA values is directly dependent on the beam width, this method also yields the beam size. Figs. 3.4a and b show the impact parameter divided by the expected errors for tracks within 100 mr of the x and y axes. These distributions are best fit by a unit gaussian when

$$\sigma_{bx}=480\pm10\ \mu$$

a)

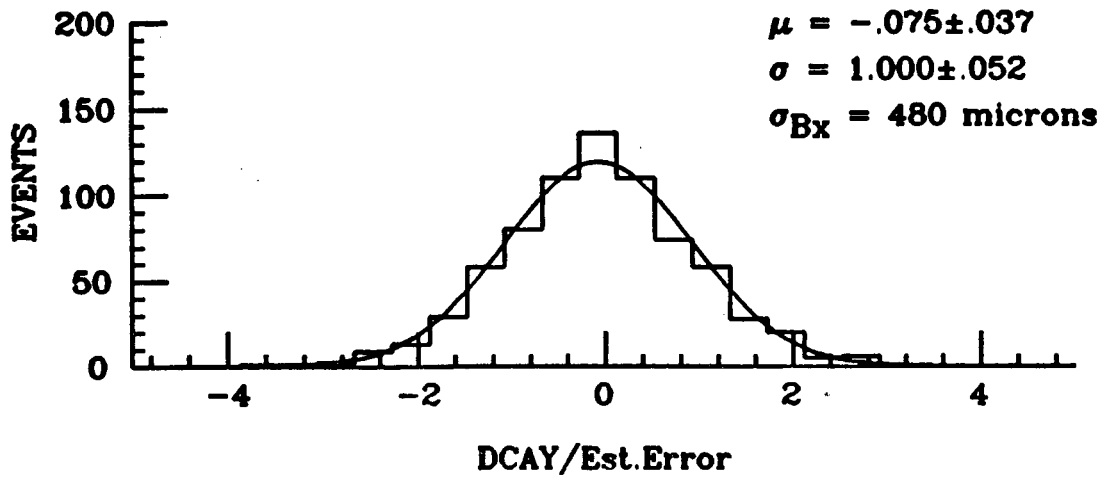

b)

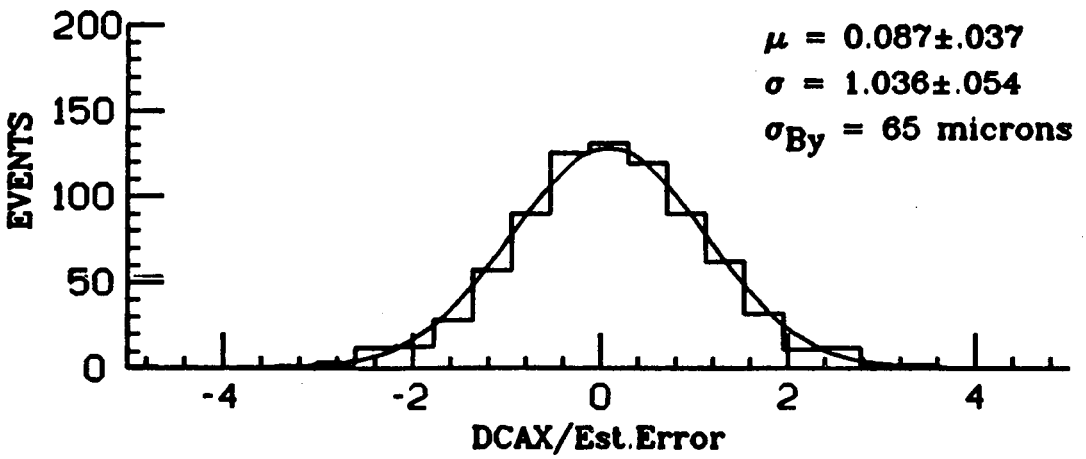

Fig. 3.4 Impact parameter to beam center in units of error
a) for horizontal tracks
b) for vertical tracks

σ_{by}=65±15 μ

The data in these plots comes from runs containing tau, charm or bottom candidates. The lack of tails in the plots indicates that the beam position was stable during these runs.

Note that for both the XYZIR and ORCALC values, the beam location error is significantly smaller than the actual beam size.

3.6 Checks on VC performance

Isolated electrons from Bhaba scattering are unencumbered by the problems of multiple coulomb scattering and tracking confusion; as such, they provide a powerful probe of the reliability of VC tracking.

In one test, tracks are grouped in azimuth according to which wire in the inner VC layer was hit. The mean impact parameter to the XYZIR origin for each group is plotted vs. wire number in fig. 3.5. Sinusoidal variations in this plot would indicate a net displacement of the detector or beam from the XYZIR origin. No such modulation is seen. More importantly, other systematic variations would indicate deviations from azimuthal symmetry arising from geometrical misalignments. Azimuthal symmetry is crucial to the lifetime analysis because it cancels, to first order, many obvious sources of systematic error (thus, even if our beam positions suffered a net displacement, lifetimes on one side would be too long, lifetimes on the other side would be too short, and the effect would cancel). Large deviations of this kind are also absent; we conclude that all azimuthal regions point back to the same

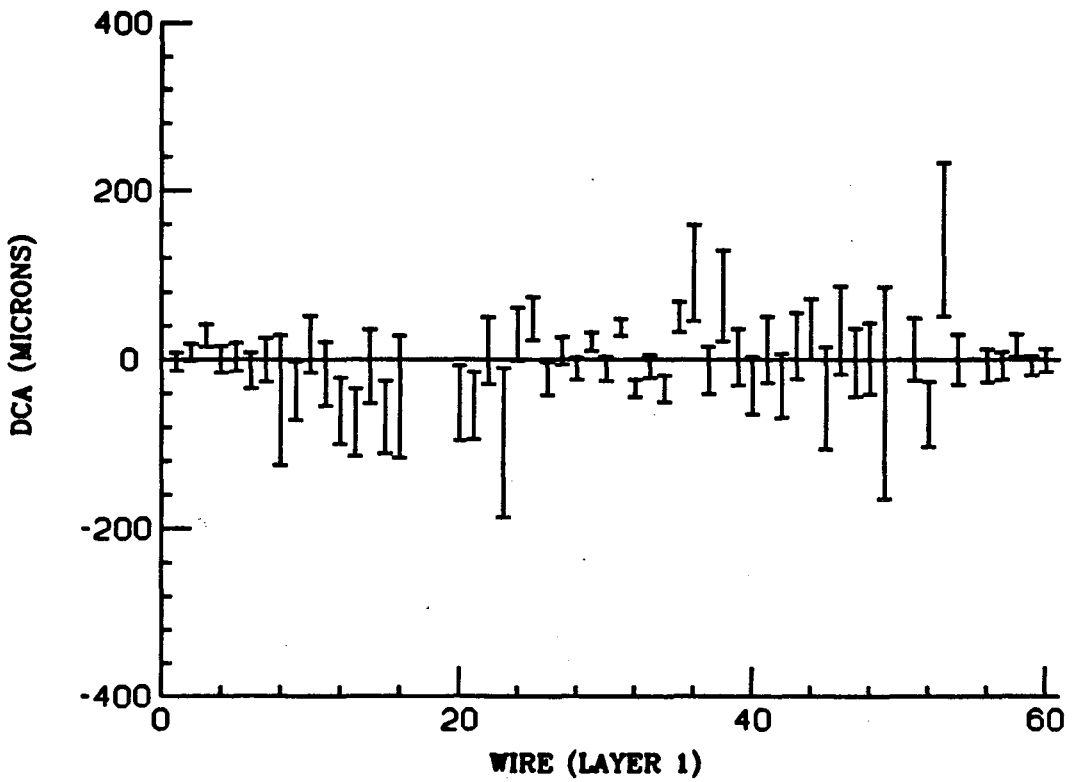

Fig. 3.5 Impact parameter to beam origin vs. azimuth
(azimuth measured by wire number in inner layer)

spot with an accuracy of 40μ or less. (The gap near wire 20 corresponds to a small region afflicted with a high voltage problem and not included in this study.)

Another test looks at the separation distance between the two bhaba tracks in the vicinity of the origin. The distribution of this quantity is shown in fig. 3.6; it is a nicely centered gaussian with width 141 μ. Since the tracks actually originate from the same point, the width should be $\sqrt{2}$ times the extrapolated tracking error discussed in chapter 2; this figure then indicates that

$$\sigma_{ex} \simeq 100\mu$$

Recall that the considerations of chapter 2 predicted a value of 85 μ for this resolution. Part of the discrepancy lies in the fact that the tracks used in this study do not necessarily have hits in all seven layers, degrading the accuracy of the extrapolation to some degree (recall eqn 2.1). Beyond this, the message contained in this result is that there are components to the tracking error which we have <u>not</u> anticipated. This issue will be studied in detail in chapter 5.

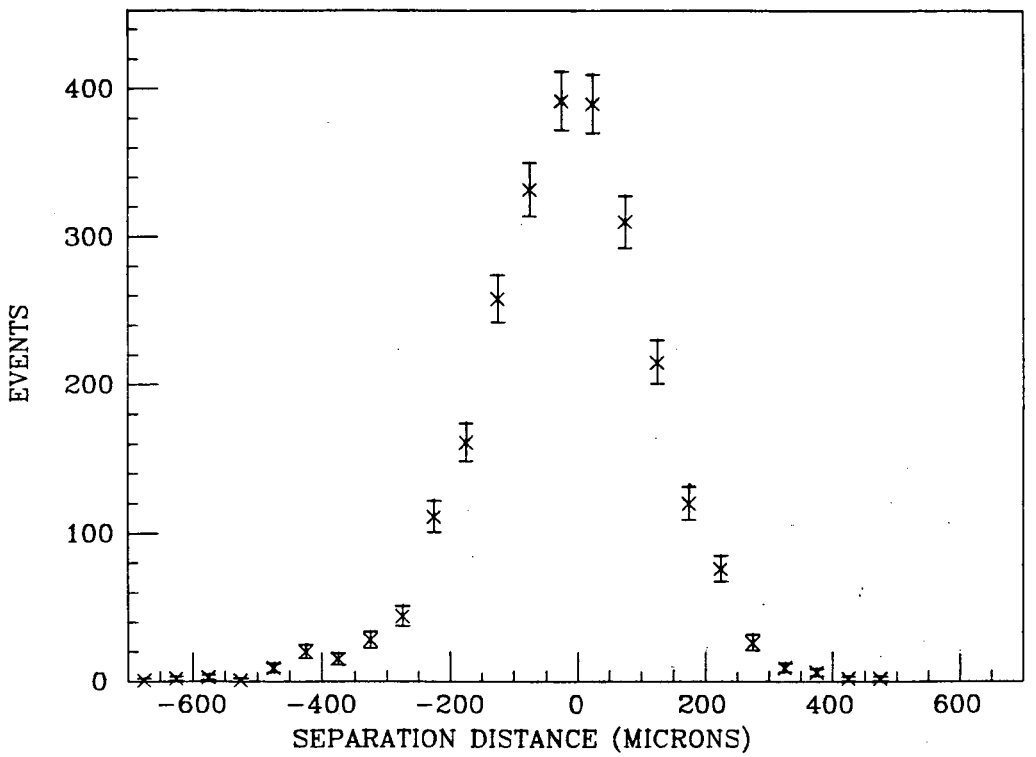

Fig. 3.6 Extrapolated miss distance of bhaba tracks

4. MEASUREMENT OF THE MEAN TAU PATH LENGTH

Once the vertex detector is operational, installed in the Mark II at PEP, the data recorded, and the events analyzed and stored on magnetic tape, we can consider the measurement of the tau lifetime. This measurement is based on 134 pb^{-1} of data collected at PEP between September 1981 and June 1983. The measurement, as well as the discussion following, is based on the general procedure outlined in sec. 1.2.

4.1 Event Selection.

Since the tau decay products always include at least one neutrino, it will not be possible to select them using the usual criterion for particle identity, the invariant mass. Instead, I will argue quite generally that tau decays at PEP can be tagged via a characteristic topology. I will then discuss additional fine tuning cuts, and some checks that the sample is truly tau's.

Recall that the lifetime will be measured by calculating the displacement between the tau's production point and decay vertex. Event selection then focuses on the 3 prong decay mode. As the tau is produced at the beam energy, we expect the 3 pions from this decay to be collimated into a narrow cone.

Now consider the overall structure of a tau pair event containing at least one such 3 prong decay. With the exception of the possible miniscule branching fraction into 5 prongs ($\leq$ 0.6%) [16], the tau decays exclusively into either 1 or 3 prongs. The tau pairs of interest are

then limited to two topologies: 1 prong opposite a collimated 3 prong jet, or back-to-back 3 prong jets. I thus isolate a crude "tau-like" sample by requiring either

> 4 charged tracks, with 1 track isolated from the other 3 by 120^0
>
> or
>
> 6 charged tracks falling into two 3 track clusters, with each member of one cluster isolated from each member of the other by 120^0

In order to discriminate against garbage events produced by beam gas scattering and other gross backgrounds, the overall vertex of each event was required to lie close to the luminous region, with an allowed miss distance of 2 cm in the xy plane, and 5 cm along the beam line. In addition, each event was required to have total charge zero.

Events passing these cuts were retracked with ADDTC as per the prescription discussed in chapter 3. The retracked tau candidates were then subject to further cuts tailored to reject background specific to these topologies:

i) low multiplicity hadrons

Including geometrical losses, the average charged multiplicity at E_{cm}=29.0 Gev is $\langle n_{ch} \rangle$=9, compared with the maximum of 6 charged tracks allowed by the topology cuts. Hadron contamination should therefore be quite small. I nevertheless protect against low multiplicity hadrons

by examining the mass of the tau-like system. I first calculate the mass of the charged prongs alone. From the work of the Mark II at SPEAR, the mass of this decay channel is known to be approximately 1.10±0.3 Gev [17]. Allowing a little more leeway than the quoted width, I therefore require

$$0.7 \text{ Gev} \leq m_{3\pi} \leq 1.5 \text{ Gev}$$

To protect against the possibility of chance charged mass combinations in this region, I also calculate the mass of the tau-like system including neutral energy. For this purpose, I include hits in the liquid argon system registering more than 300 Mev, provided they are within 60^0 of the 3π direction. The tau mass is 1.784 Gev. I allow for the possibility of some mismeasurement, and require

$$M_{3\pi+\text{neutrals}} \leq 2.0 \text{ Gev}$$

Note that failure of either jet in a 6 prong event results in the exclusion of the entire event.

ii) tau production in 2 photon collisions

The diagram for this process is shown in fig. 4.1. The cross section at 29 Gev, integrated over the detector acceptance, is ≈ 0.9 nb, which is almost as large as the pointlike cross section at this energy. Unfortunately, the cross section peaks at the tau pair threshold, leading to tau's which are at rest (or close to it) in the lab frame. These have a smaller gamma factor, and thus a shorter mean path length,

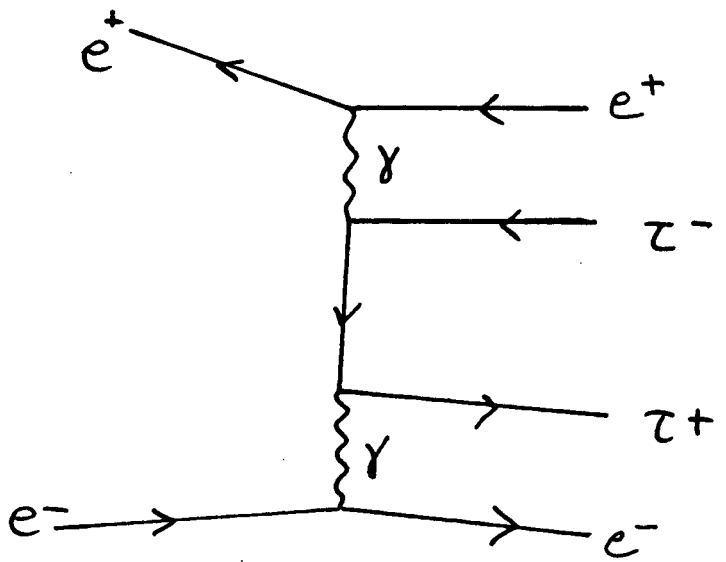

Fig. 4.1 Tau production in two photon collision

than tau's produced at the beam energy, and therefore constitute a background to the scheme of this measurement.

Removal of these 2γ tau's hinges on their slowness. I look at the total charged energy in the event, and the energy of each 3π system, and require

$$\text{total } E_{ch} \geq 5.0 \text{ Gev}$$

$$E_{3\pi} \geq 3.0 \text{ Gev}$$

Using the total energy to discriminate against 2 photon events is actually standard operating procedure in e^+e^- physics. In fact, events stored in the Mark II data summaries are all required to have

$$\text{total } E_{ch} \geq 3.6 \text{ Gev}$$

The cuts above merely amplify this requirement.

One further distinguishing feature of 2 photon events is the fact that they tend to have a net component of momentum along the beam direction. Some of these events are thus eliminated by the topology cut, since it requires (rather loosely) that the tau decay products appear to recoil against each other in the detector.

iii) radiative bhabas and dimuons

Bhaba events, and to a lesser degree dimuons, are sometimes accompanied by bremsstrahlung in the final state. The photon direction is usually quite close to that of the emitting lepton; if this photon converts close to the beam line, the net effect is to produce a collimated

3 prong jet in the tracking volume. If the lepton on the other side does not radiate, the event will mimic the 4 prong tau pair topology; if both leptons radiate, and both photons convert, the event can mimic the 6 prong topology. One way to eliminate this background is to note that the charged tracks in such an event will carry the full center-of-mass energy. A real tau pair, however, will contain two or three undetected neutrinos, and show a corresponding missing charged energy. To eliminate radiative events, I therefore require

$$\text{total } E_{ch} \leq 26.0 \text{ Gev.}$$

An alternative technique is based on the kinematics of the radiative 3 prong system. The photon is massless, the radiating lepton is almost massless, and the angle between them is small. The effective mass of such a system will also be small. Three collimated pions, however, cannot have an effective mass less than $3m_\pi$. Assuming that the photon converts to an electron-positron pair, I calculate the mass of each 3 prong using the electron mass for all particles, and require that it be somewhat less than $3m_\pi$:

$$m_{3e} \leq 0.3 \text{ Gev}/c^2.$$

A further cut against this kind of background will be discussed in the next section.

This completes the tau selection criteria. Since no one requirement actually specifies any event as a tau, it is necessary to check that the kinematic properties of the final data set are consistent with the known properties of the tau. This is most easily done by comparison

a)

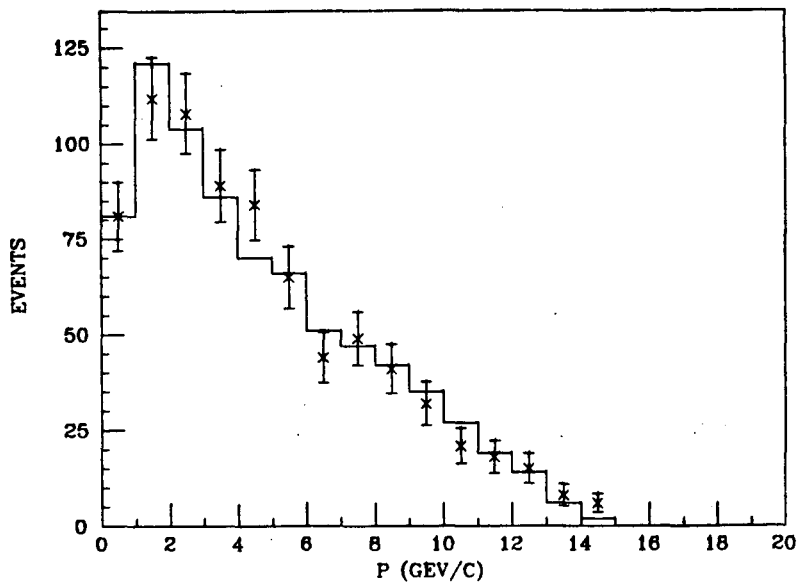

b)

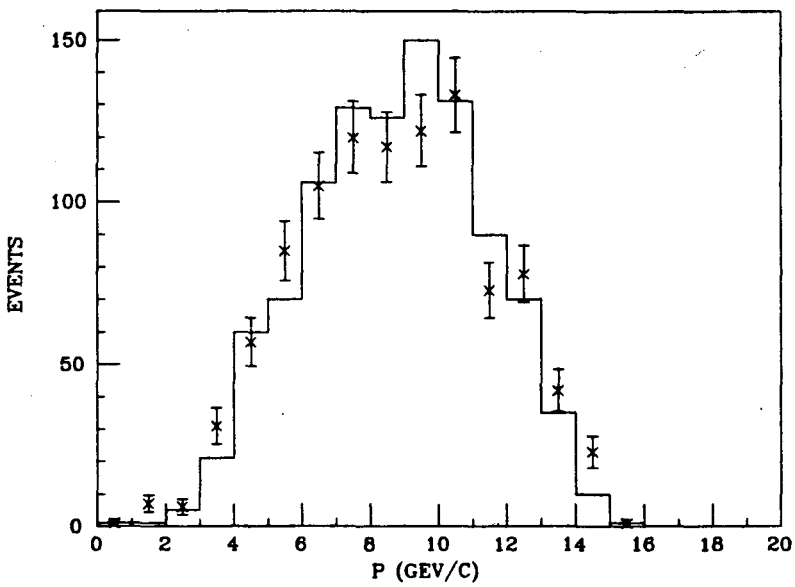

Fig. 4.2 Comparison of momentum spectra in data (x) and Monte Carlo (solid curve).
a) for 1 prong tau decays
b) for 3 prong tau decays

with the Monte Carlo. In fig. 4.2a, I show the momentum spectrum of the isolated single prongs in the passing 4 prong events. The solid curve is the result of the Monte Carlo. The agreement is quite good. In fig. 4.2b, I compare the momentum spectrum of the passing 3 prongs with Monte Carlo expectations; the agreement here is also impressive. A "typical" four prong event, as seen in the full detector, is shown in fig. 4.3a; a magnified view of the VC portion of the event is shown in fig. 4.3b. Confident of the validity of the tau sample, I now move on to the discussion of event quality.

4.2 Selection of well measured events. Vertexing.

A precision measurement of this kind requires that tails are minimal and that the "resolution function" is understood. To this end, I now impose a series of cuts which insure the fidelity of the tracking information in the final sample. The strategy here is to impose an interlocking, unbiased requirements which eliminate gross tails, while preserving statistics. From this point on, each 3 prong tau decay is treated as an individual.

A simple starting place is to beware of tracks with small momenta. These tracks have a high probability of scattering, producing kinked trajectories, delta rays, and secondaries, all the bane of good tracking. Furthermore, a track scattered in the beam pipe is obviously useless for the purpose of extrapolating back to the τ decay point. To avoid these problems, I therefore require that all tracks in a passing 3 prong have

a)

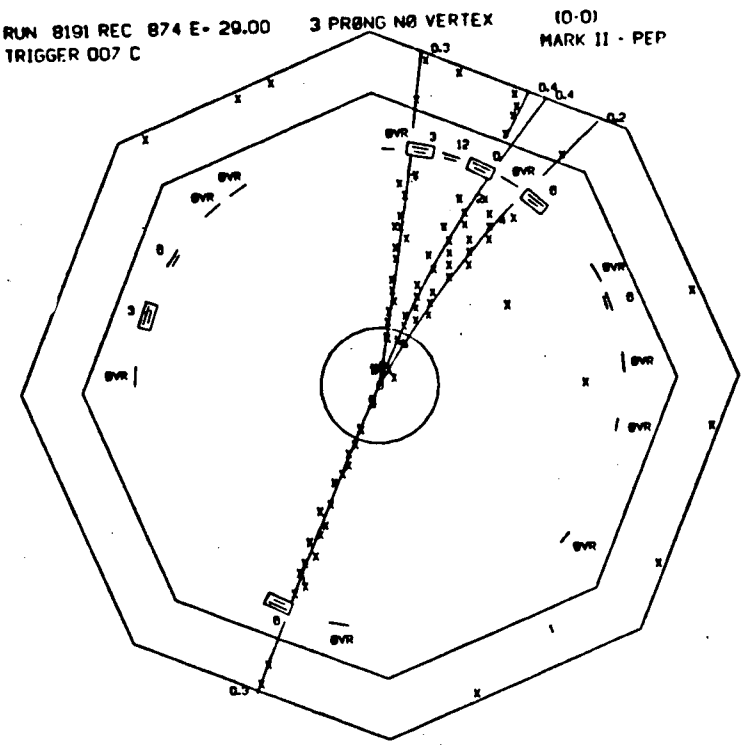

b)

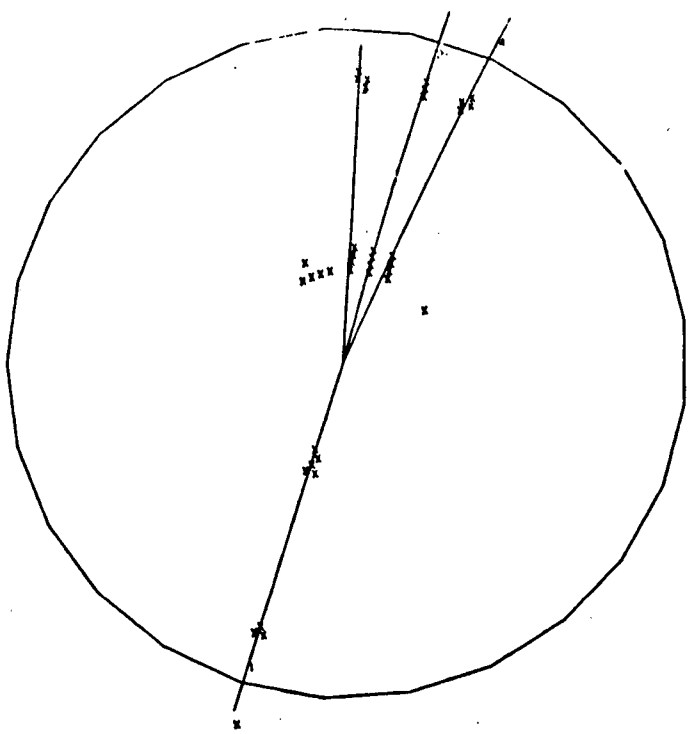

Fig. 4.3 A 'typical' tau event
a) full view in the Mark II
b) magnified view in the vertex detector

$p_{tr} \geq 0.400$ Gev/c

Now consider actual tracking quality. Tracks are the result of a least squares fit to the measured data points; a good track will require a minimum number of points. To insure a good extrapolation to the origin, as well as optimal use of the VC information, I require that each of the three prongs have at least 2 hits in the VC inner band, and at least 1 hit in the VC outer band. Since there is little intervening material between the IP and the active VC elements, this requirement also eliminates radiative bhabas and mu pairs in which the photon converts at the VC/DC interface.

To insure a good curvature measurement, I require that each track also have at least 6 hits in the main DC. This is a rather minimal requirement, aimed at preserving statistics in an era where the DC was showing its age; it is not sufficient to insure good dip information. This task will fall to the vertex χ^2, to be discussed shortly.

A good track also requires a good fit to the data points. The most straightforward measure of "goodness of fit" is the track χ^2. As discussed in chapter 3, the χ^2 per degree of freedom measures the rms of the tracking residuals in units of the tracking errors:

$$\chi^2_{pdf} = (N-5)^{-1} \sum_i \frac{(d_{fit}-d_{meas})^2}{\sigma_i^2}$$

An error in tracking will usually lead to one or more large residuals, and an anomalously large χ^2_{tr}. But this measure is dependable only if one knows the σ_i's to be correct; since the VC σ_i's were derived from

mostly bhaba type events, there is no guarantee of their correctness in the somewhat denser tracking environment of the tau's. To check, I plot in fig. 4.4a the distribution of χ^2_{tr} for tracks in the tau sample that carry the full complement of 7 hits in the VC. Recall, from chapter 3, that this should be the χ^2 distribution for 5 degrees of freedom. The data appears wider than expected, suggesting that the bhaba derived VC σ_i's are a little small. The proof of this suggestion is fig. 4.4b, which shows the same sample refit with all VC σ_i's multiplied by 1.15. The agreement between data and theory is now acceptable.

The implication of this exercise is that the VC resolution is somehow degraded by a factor of 15% in the denser tau events. One cause of this may simply be confusion between tracks during pattern recognition. Alternatively, it may be that the simultaneous firing of many nearby wires generates pickup which degrades the resolution on any one channel. Whatever the cause of the disease, it seems that this average kind of rescaling is an adequate treatment; for the remainder of this work it should be assumed that all events have been refit with the VC σ_i's increased in this way.

Let the chisquare per degree of freedom for the entire track be denoted as χ^2_{tr}, and the chisquare per degree of freedom for the VC information alone as χ^2_{vc}. The distribution of these quantities in the tau data is shown in fig. 4.5. Each track in a passing 3 prong is required to have:

$$\chi^2_{tr} \leq 4.0$$

a)

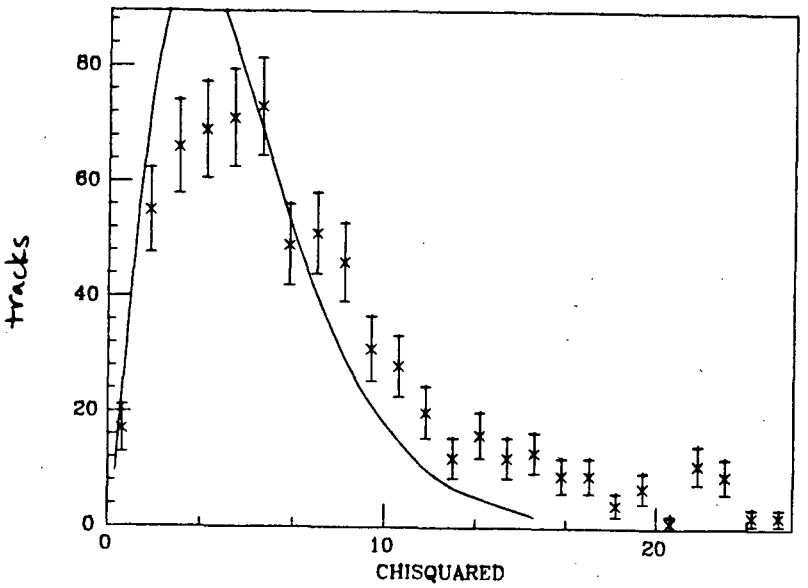

b)

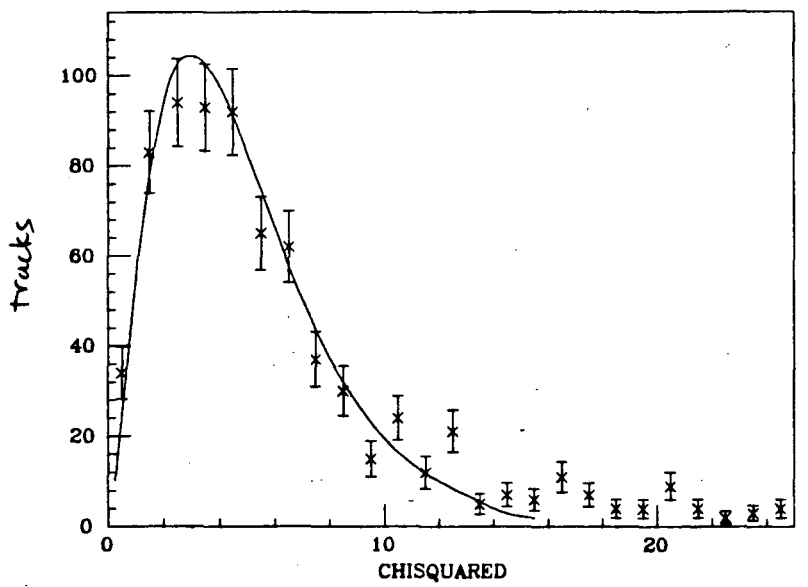

Fig. 4.4 Single track χ^2 in the tau sample
a) using the standard tracking errors
b) with tracking errors increased by 15%

a)

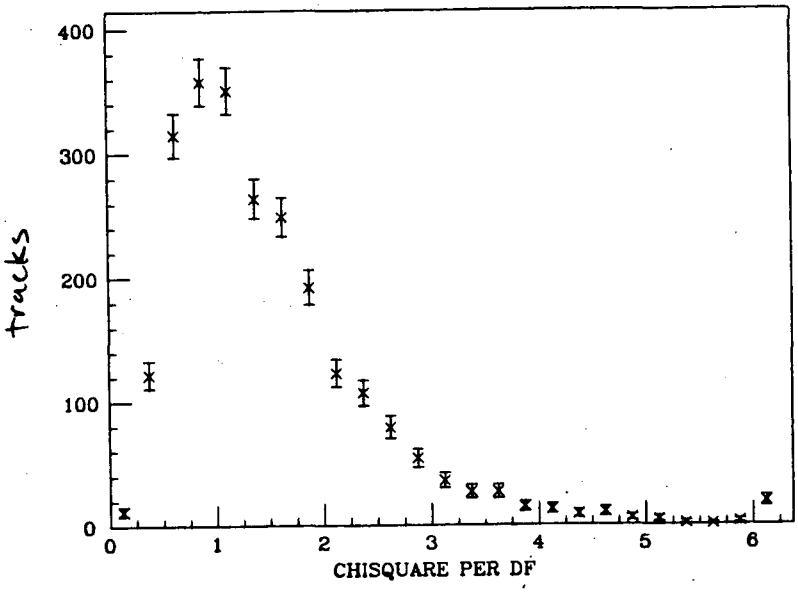

b)

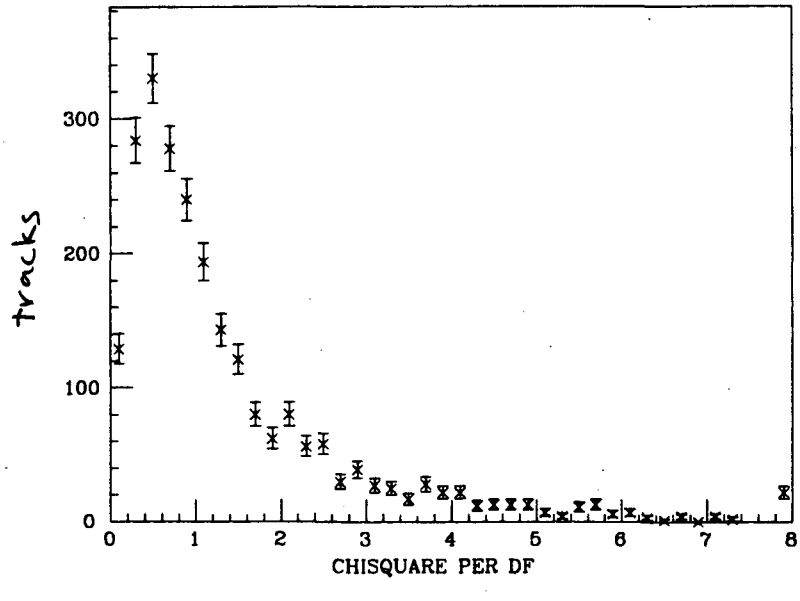

Fig. 4.5 Track χ^2 per degree of freedom
a) in the combined VC+DC system
b) in the vertex detector alone

$$\chi^2_{vc} \leq 5.0$$

These cuts are lenient, but do remove a number of gross delinquents.

One reason for keeping track χ^2 cuts rather loose is the fact that one bad time can sometimes make the χ^2 large while actually having little effect on the track parameters. This tends to occur for tracks with a large number of hits. Alternatively, for tracks with a small number of hits, a fortuitous combination of errors in the pattern recognition can sometimes produce a track which is hopelessly wrong, but nevertheless has a good χ^2. These later kinds of errors can be flagged by checking to see that the track points correctly back to the known beam position. This procedure also spots tracks which have scattered in the beam pipe.

For each track, I calculate the distance of closest approach (DCA), in the xy plane, to the beam center. The finite tau lifetime, along with the finite beam width, will give some contribution to the width of this distribution. Using an average decay product opening angle of 0.3 mr (see fig. 5.3a), and the canonical lifetime, it is easy to calculate that the average miss distance from the nonzero flight path is about 200 μ. Combining this in quadrature with the maximum beam width of 500 μ in the x direction, we get an order of magnitude estimate of the mean DCA to be about 550 μ. Checking the tau sample, in fig. 4.6, I find this estimate nicely duplicated by the data, with only two tracks in the sample having a DCA greater than 2mm. I conclude that this pathology has already been eliminated by the requirements on minimum number

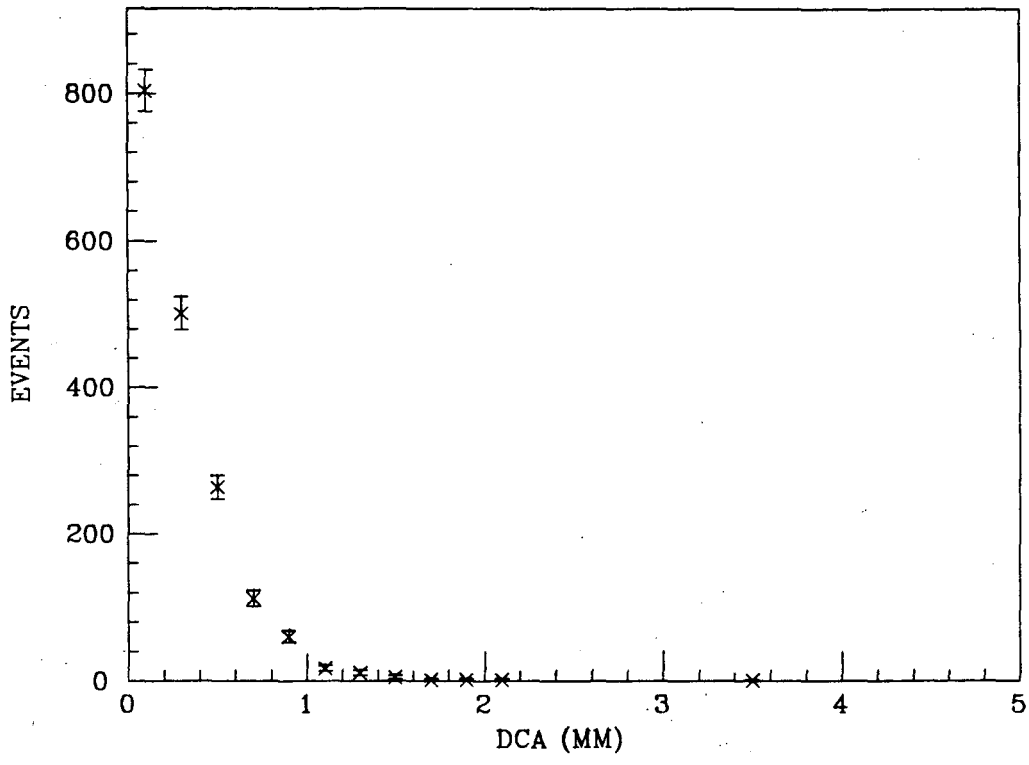

Fig. 4.6 DCA of tau tracks to beam center

of hits and minimum momentum.

The foregoing battery of quality cuts yields 594 passing 3 prongs. These candidates are now refit with the constraint that all 3 tracks originate from a common vertex, the putative tau decay point. The vertex constrained fit proceeds by a χ^2 minimization, and returns new track parameters, vertex location, vertex error ellipsoid, and the vertex χ^2. This latter quantity measures the dispersion of the tracks at their point of closest approach, in units of the assumed tracking and multiple coulomb scattering errors. Through the assumption that the tracks do have a common origin, it is another strong check on tracking quality. In fig. 4.7a, I display the distribution of χ^2_{vtx} in the tau sample. For a 3 track vertex, there are 3 degrees of freedom; the solid curve is the theoretical expectation for this case, normalized to the number of events with $\chi^2_{vtx} \leq 20$. The disagreement is embarrassing. The same comparison made with Monte Carlo data gives a very nice fit,indicating that the problem does not originate with any kind of error in the vertexing algorithm. We might consider rescaling the tracking errors, but they have already been adjusted to bring the VC track χ^2 into line, as per above. The problem must therefore lie with the information used in track reconstruction.

The vertex is a point in 3-dimensional space. Information on the xy coordinates of this point comes mainly from the VC, whereas the z coordinate results solely from DC information. To disentangle these contributions, I revertexed the sample with track z errors increased by a

a)

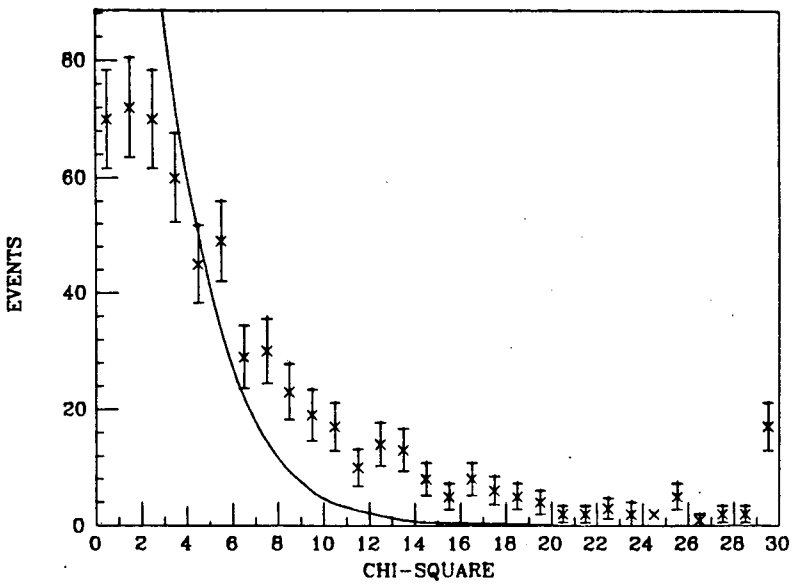

b)

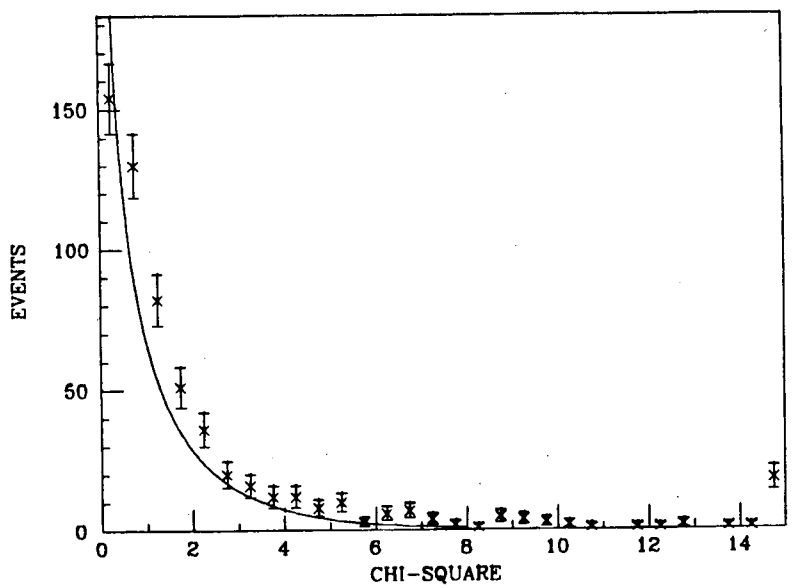

Fig. 4.7 Vertex χ^2
a) for reconstruction in three dimensions
b) for reconstruction in the xy plane only

factor of five, effectively removing the z information from the fit. This reduces the problem to that of finding a vertex in xy projection; for three tracks, such a fit has 1 df. The resulting χ^2_{vtx} is shown in fig. 4.7b, along with the theoretically expected curve. The improvement over fig. 4.7a is obvious. This implies that the xy part of the vertexing is healthy, and that the problem must lie with the z information from the DC.

In fig. 4.8, the problem is recast in a zy projection. Let y_0 be the y coordinate of the vertex as determined by the procedure above. In the absence of perfect z information, the three tracks will intersect the line of constant y_0 in three different places. Assuming equal errors, the best estimate of the z point of the decay is just the average z of the three intersection points. Then, the χ^2 of the z information alone is given by:

$$\chi^2_z = \sum_{i=1}^{3} \frac{(z_i - z_{av})^2}{\sigma_{zi}^2}$$

The distribution of this quantity is shown in fig. 4.9, along with the normalized theoretical expectation for 2 df. The poor agreement mimics fig. 4.7a, implying that faulty z information <u>is</u> the culprit. Requiring a large number of hits in the DC cleans up the low end of this distribution to some degree, but the long non-gaussian tail still remains.

As in the treatment of the track χ^2 difficulties, I chose to avoid an extensive exploration of the causes of this tail. Since the vertex precision is so dependent on the VC anyway, it appears best to simply

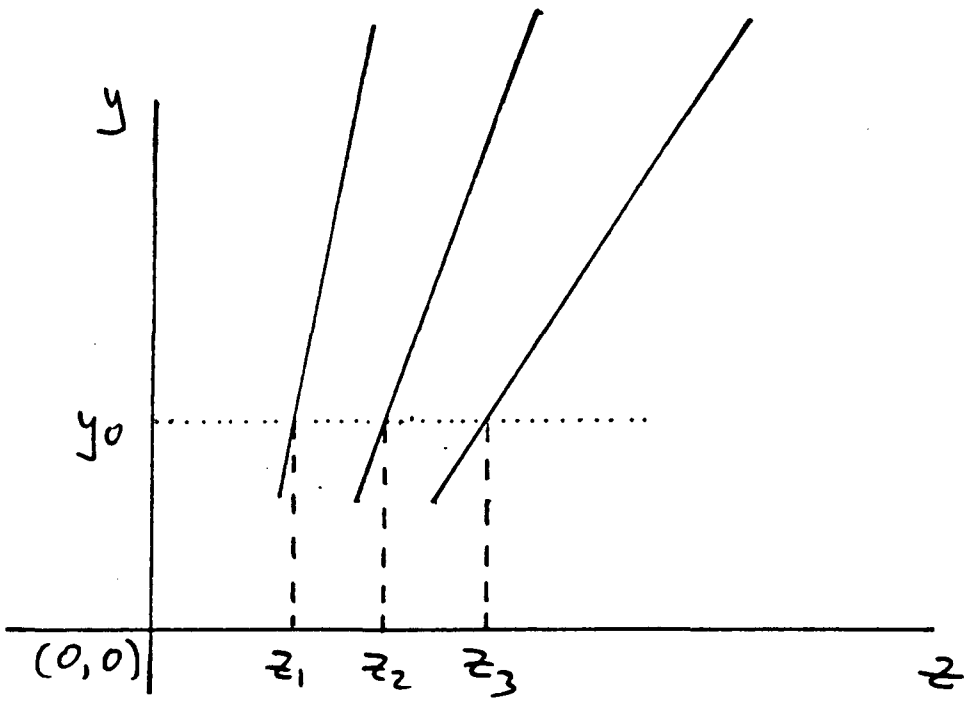

Fig. 4.8 A hypothetical 3 prong decay in zy projection near the origin

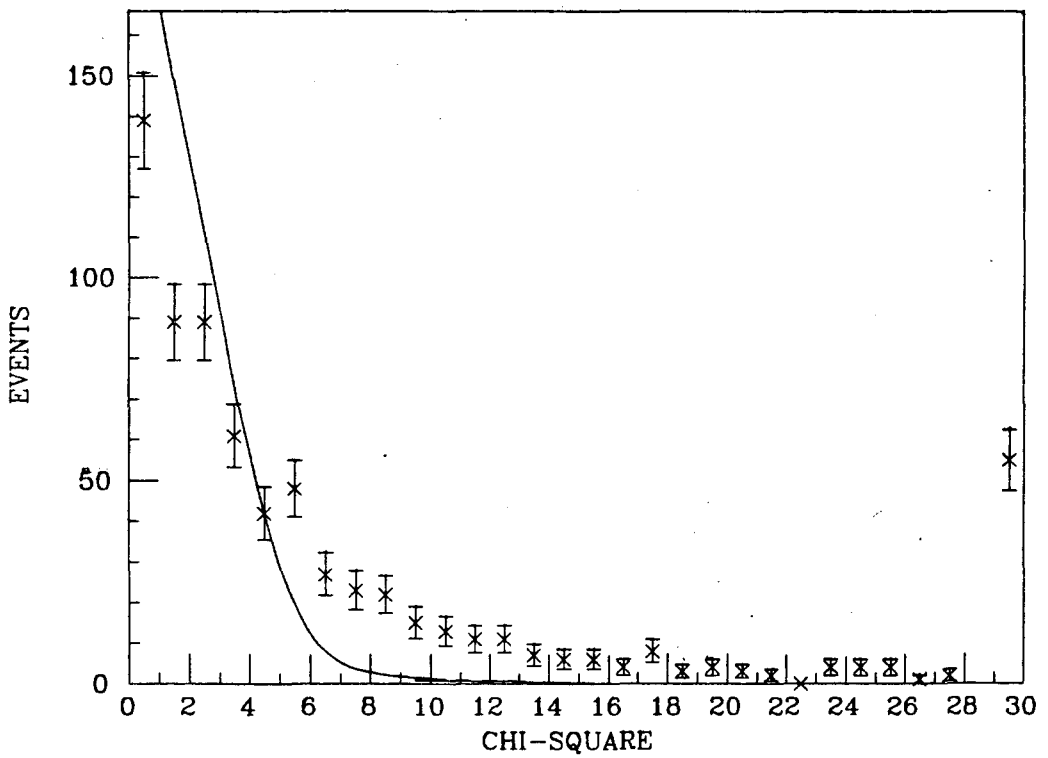

Fig. 4.9 The z contribution to the vertex χ^2

remove the z information as outlined above. All of the 3 prongs were vertexed in this fashion. The extraneous noise is then excluded, and χ^2_{xy} stands as a strong overall summary of the quality of the xy vertex information from the VC. With this in mind, the cut on the vertex χ^2 is rather strict:

$$\chi^2_{xy} \leq 4.0$$

It is hard to draw conclusions about χ^2_z, because of the unknown drift chamber problem which leads to this rather rude distribution. Fortunately, the calculation of the tau path length will be seen to be rather insensitive to the quality of the z information. Nevertheless, as a very large value for χ^2_z, could indicate a real tracking problem I exclude the far tail:

$$\chi^2_z \leq 20.0.$$

The remaining sample contains 507 3 prong decays.

4.3 Calculation of the tau path length

The analysis discussed so far provides, for each passing tau, a best estimate of its decay point, and associated errors. Via the discussion of chapter 3, a best estimate of the beam size and beam center are also known. One easy estimate of the τ path length is now given as the distance from beam center to decay point. But such an estimate is hardly optimal, as it fails to account for the known vertex errors and beam spread.

To utilize this additional information, an additional constraint is

required, namely the direction of the tau in the xy plane. Offhand, the reconstruction of this direction would seem to be ruled out by the presence of the undetected neutrino in $\tau\rightarrow(3\pi)\nu$. Recall, however, that the tau decay to pions seems to occur through an intermediate, high mass hadronic state, which I shall generically label S_τ. The large mass of this state, about 1.1 Gev/c^2, implies that in the tau rest frame, it is created almost at rest. In fact, it is easy to show that, in this frame, the S_τ momentum is given by:

$$P_{S\tau}= \frac{M^2_\tau - M^2_{S\tau}}{2M_\tau}$$

In the lab frame, S_τ is then expected to closely follow the tau direction, with a maximum angular difference given by

$$\theta=\tan^{-1}\left[\frac{P_{S\tau}\ M_\tau}{P_{beam}\ M_{S\tau}}\right]$$
$$\simeq 3.5^0$$

If the intermediate state decays only to three charged pions, the tau direction is then given in good approximation by the direction of the 3π system. This assumption will be used in the following. The error inherent in this assumption, as well as that arising from undetected neutral pions, will be addressed by Monte Carlo techniques in sec. 6.4.

I now consider the problem of the optimal estimate of the tau decay length. I shall use beam positions as given by XYZIR, and beam sizes as given by the ORCALC calculation:

$$\sigma_{bx}=480\mu \qquad \sigma_{by}=65\mu$$

Let the beam center be given by (x_b,y_b). The beam error matrix is the

2x2 diagonal matrix whose nonzero elements are the inverse squares of the beam size in the x and y directions. Let the inverse of this matrix be B_{ij}.

Let the xy position of the reconstructed decay vertex be (x_v,y_v). Since the vertex error ellipse has a major axis which tends to lie along the tau's flight direction, the 2x2 matrix of vertex errors is non-diagonal. Let the inverse of this matrix be V_{ij}.

Finally, let the tau direction cosines in the xy plane, as approximated by the direction of the 3π system, be given by (t_x,t_y). The entire situation is summarized in fig.4.10, which shows a magnified view of the region near the origin for the event already pictured in fig. 4.3.

The best estimate of the tau flight path is a line segment satisfying three constraints:

i) one end must be optimally close to (x_b,y_b), in the sense of B_{ij}

ii) one end must be optimally close to (x_v,y_v), in the sense of V_{ij}

iii) the segment must have direction (t_x,t_y)

The optimization required by i) and ii) can be expressed in a χ^2 formalism. Let the point satisfying i) be (x,y), and the point satisfying ii) be (x',y'). The relevant χ^2 is then:

$$\chi^2=(x-x_b)^2B_{xx}+(y-y_b)^2B_{yy}+(x'-x_v)^2V_{xx}+(y'-y_v)^2V_{yy}+2(x'-x_v)(y'-y_v)V_{xy}$$

In order to incorporate the constraint iii), we express (x',y') in

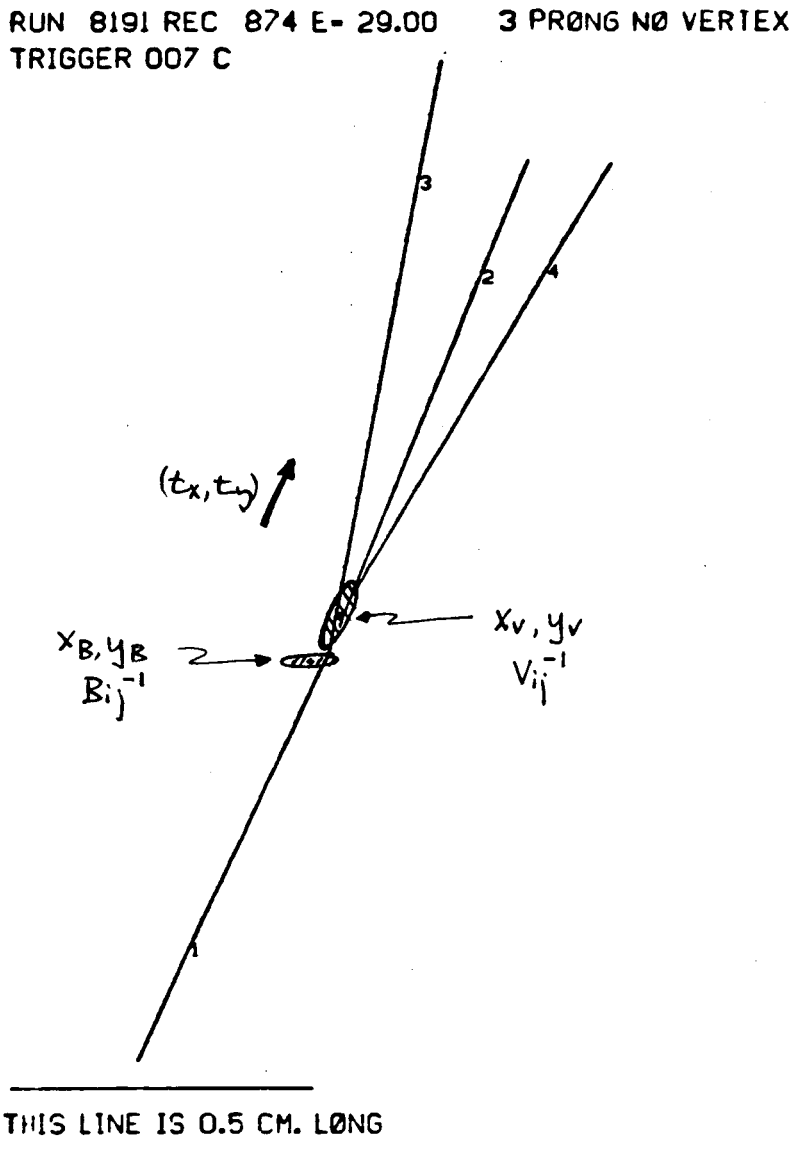

Fig. 4.10 Calculation of the tau flight path

terms of (x,y), the direction (t_x,t_y), and an unknown path length ℓ:

$$x'=x+t_x\ell \qquad y'=y+t_y\ell$$

Substitution then yields a chi square for the three unknowns x,y, and ℓ. Minimization of this χ^2 gives the best estimate of:

the tau 'production point'
with respect to the beam center (x_p,y_p)

the tau path length ℓ

In addition the matrix of second derivatives of the χ^2 is constructed and inverted, furnishing the errors in each of the three quantities. The path length error will be denoted as σ_l. Since the VC is lacking z information, ℓ and σ_l as calculated above are actually projections in the xy plane; to get the true versions, we divide by the cosine of the dip angle. This is the "weak" dependence on z information alluded to in sec. 4.2.

The distribution of σ_l is shown in fig. 4.11. This quantity varies from event to event because of two effects. One is momentum dependence: slow 3 prongs have large opening angles and well defined vertices, but large multiple coulomb scattering errors; fast 3 prongs have small scattering errors, but are rather collimated and therefore have a poorly defined vertex. The other is the rather large size of the beam in the x direction. This leads to a larger uncertainty in the location of the production point for horizontally directed tau's. The average

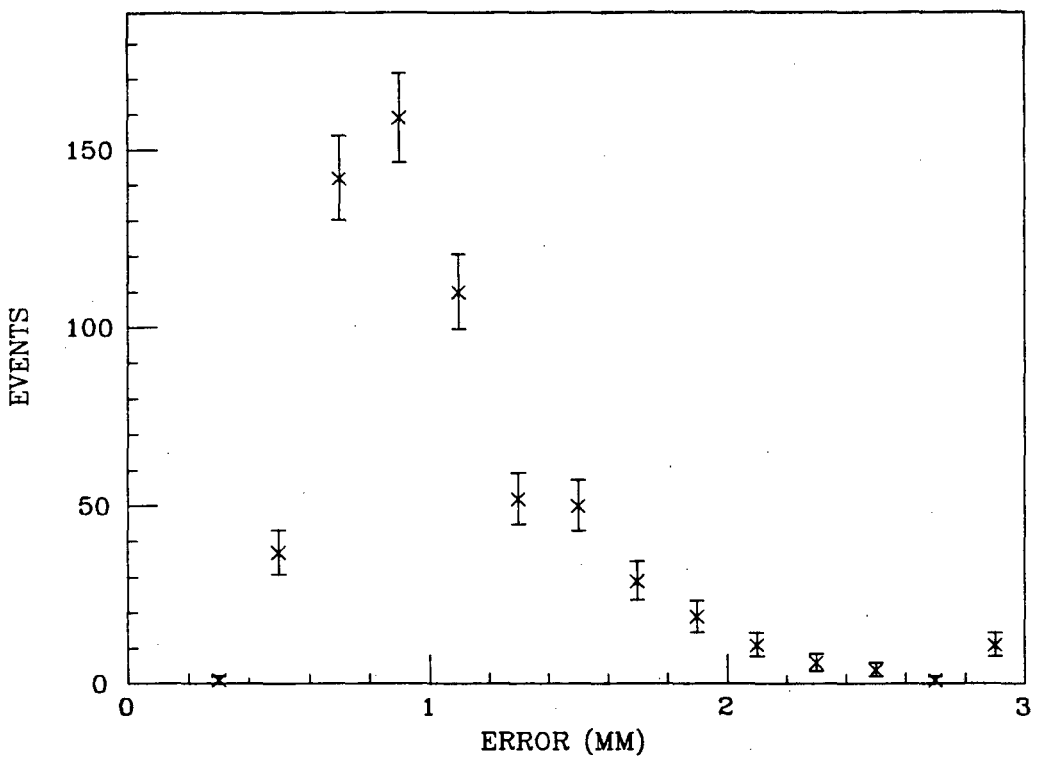

Fig. 4.11 Path length errors

is ≃ 1 mm (comparable to the size of the expected tau path length), but there is a substantial tail extending out to large errors. We will use only the 'high precision' part of the data, cutting at

$$\sigma_1 \leq 1.4 \text{ mm}.$$

The location of this cut is rather arbitrary; this issue will be treated under the discussion of systematic errors.

The distribution of production points, shown in fig. 4.12, is a kind of time average of the beam profile. The enables a nice quality cut: tau's whose apparent origin is outside of the beam are either mistracked or have bad beam positions. We require that both x_p and y_p lie within two sigma of (x_b, y_b).

The σ_1 and production point cuts leave 423 events in the final sample. The distribution of path lengths is shown in fig. 4.13. This plot is rather striking; it clearly shows an exponential with width about 1mm folded with a gaussian error function whose width is also about 1 mm. Note that this analysis has avoided any kind of explicit cut on large path lengths; the relative absence of tails is then a pleasing vindication of the obsession with event quality. The mean of this distribution is 627±65 μ. Tau vixit! A more precise determination of the mean path length is derived from maximum likelihood analysis, to which I now turn.

4.4 Maximum likelihood extraction of mean path length

The maximum likelihood technique can be applied in statistical

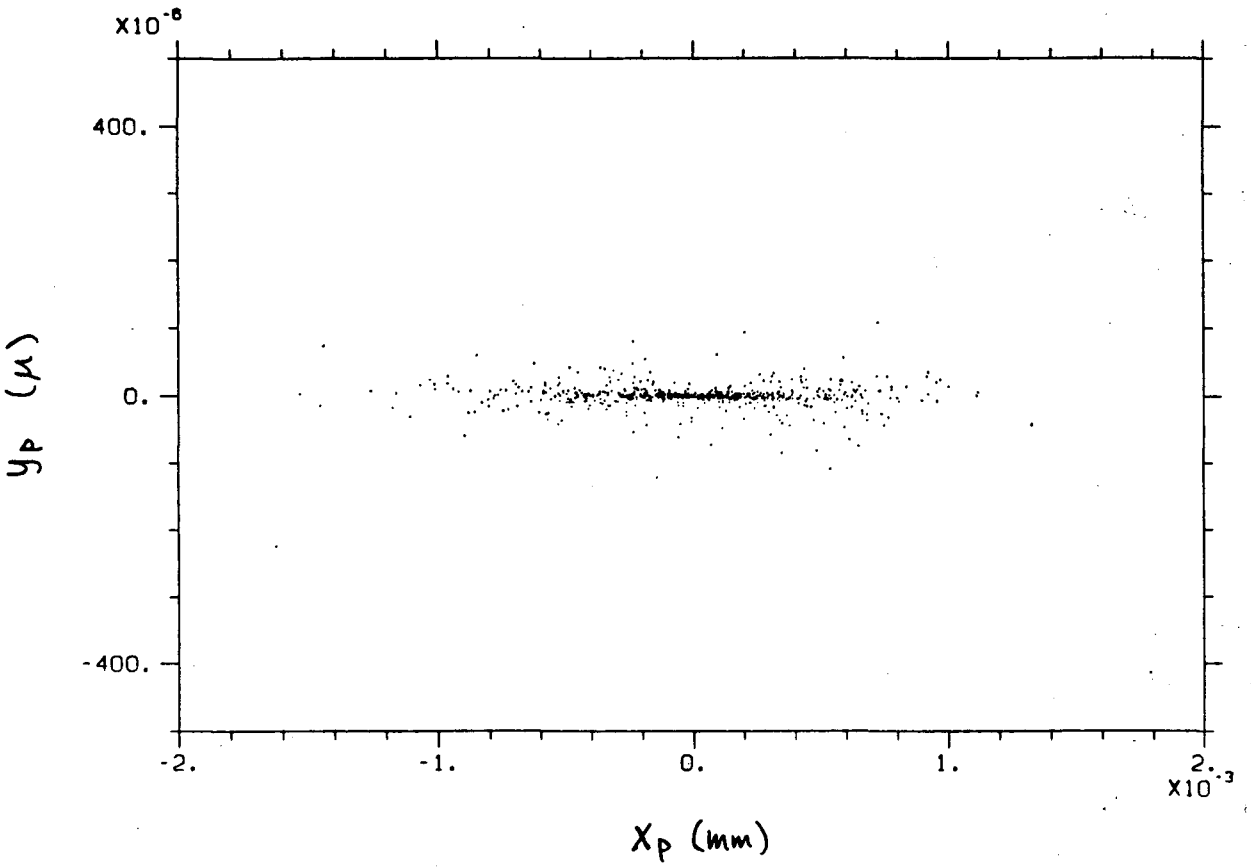

Fig. 4.11 Calculated tau production points with respect to (x_b, y_b)

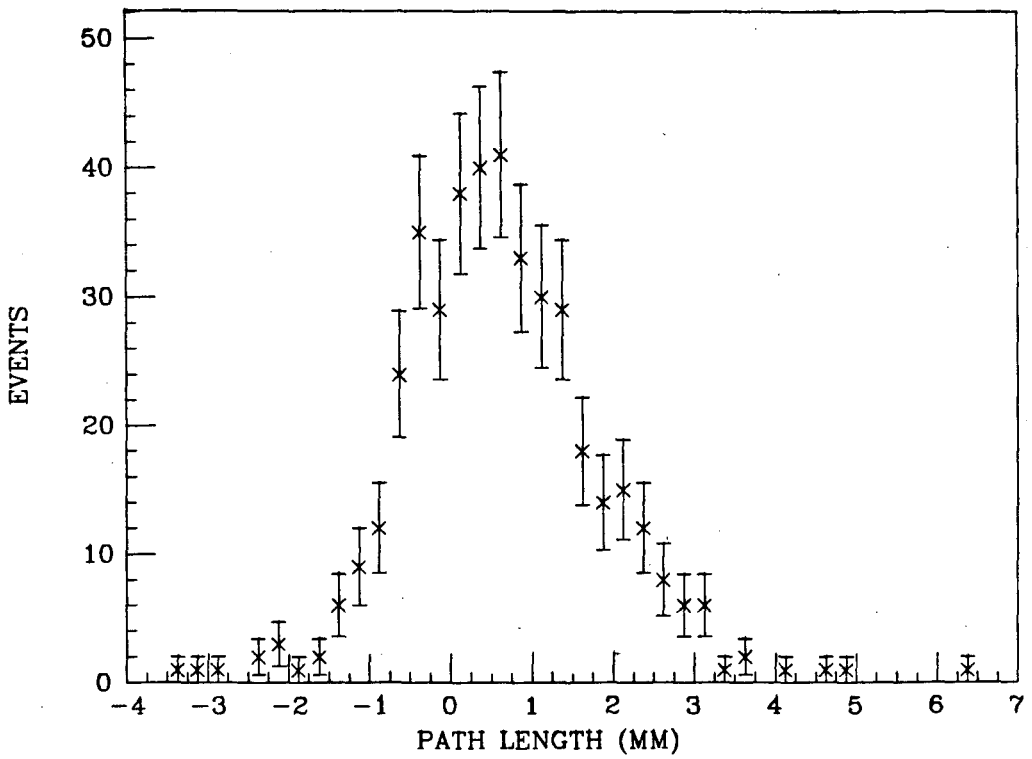

Fig. 4.13 Tau path lengths

problems where the functional form of the distribution is known. The functional form is used to calculate the overall probability of making some sequence of observations, and the best estimate of the parameter of interest is the value that maximizes this probability. It can be shown that this technique yields parameter estimates with the minimum attainable variance [25]. This happy property follows from the fact that the maximum likelihood estimator is <u>sufficient</u> : it exhausts the experimental data of all information relevant to the desired parameter.

Consider a series of N tau flight path measurements. Let the true lifetime be ℓ_0, and let the probability of observing a path length ℓ_i be given by $P(\ell_i,\ell_0)$. The total likelihood for a collection of N ℓ_i's is

$$\mathcal{L} = \prod_{i=1}^{N} P(\ell_i, \ell_0)$$

In order to prevent this product from growing unreasonably small, it is customary to use the "log-likelihood":

$$\ln \mathcal{L} = \sum_{i=1}^{N} \ln \left[P(\ell_i, \ell_0) \right]$$

The best estimate of ℓ_0 is the value at the extremum:

$$\frac{\partial}{\partial \ell_0} \left[\sum_{i=1}^{N} \ln \left[P(\ell_i, \ell_0) \right] \right] = 0$$

In a world with no measurement error, $P(\ell_i,\ell_0)$ would be the normalized exponential decay distribution with mean ℓ_0. In the real world,

however, the path lengths are smeared by the finite experimental resolution: we observe a path length ℓ_i and an error on that path length σ_1. It is therefore necessary to construct a $P(\ell_i,\sigma_1,\ell_0)$ which accounts for this.

One method would be to assume an average "resolution function" for the entire data set. This might be a gaussian whose width was equal to the average σ_1. $P(\ell_i,\langle\sigma_1\rangle,\ell_0)$ could then be represented as the convolution of the exponential of mean ℓ_0 with this gaussian.

The shortcoming of this approach is the use of a fixed σ_1; in the data, σ_1 varies from event to event. To more carefully model the situation, we can consider the measured σ_1 of a given event as the mean width of a geometry and momentum dependent gaussian resolution function associated with that (type of) event. The probability of observing such an event can then be represented as the convolution

$$P(\ell_i,\ell_0,\sigma_{\ell_i}) = \frac{1}{\ell_0}\frac{1}{\sqrt{2\pi\sigma_{\ell_i}^2}}\int_0^\infty e^{-t/\ell_0}\, e^{-(t-\ell_i)^2/2\sigma_{\ell_i}^2}\, dt$$

$$= \frac{1}{2\ell_0}\exp\left[\frac{\sigma_{\ell_i}^2}{2\ell_0^2}-\frac{\ell_i}{\ell_0}\right]\left[1-\mathrm{erf}\left(\frac{1}{\sqrt{2}}\left(\frac{\sigma_{\ell_i}}{\ell_0}-\frac{\ell_i}{\sigma_{\ell_i}}\right)\right)\right]$$

A study of systematic effects utilizing a control data sample, to be discussed in the following chapter, will require the ability to measure very short lifetimes ($\ell_0<100\mu$). Unfortunately the expression above is numerically untenable in the limit $\ell_0\ll\sigma_1$. (Recall that the average σ_1 is of order 1 mm.) In order to develop a suitable substitute, note

that the sufficiency of the maximum likelihood technique is equivalent to saying that the parameter estimation follows from the shape of the experimental distribution. Consider the shape of the gaussian/exponential convolution in the $\ell_0 \ll \sigma_1$. The mean remains at ℓ_0, the width remains at $\sqrt{(\ell_0^2+\sigma_1^2)}$, but the exponential tail becomes irrelevant compared to the gaussian width. The distribution therefore tends to a gaussian of mean and width as given above. In the short lifetime regime, we therefore take the probability of an event with ℓ_i, σ_1, and ℓ_0 to be

$$P(\ell_i, \ell_o, \sigma_{\ell_i}) = \frac{1}{\sqrt{2\pi(\sigma_{\ell_i}^2 + \ell_o^2)}} \; e^{-\frac{(\ell_i - \ell_o)^2}{2(\sigma_{\ell_i}^2+\ell_o^2)}}$$

The practical use of these formulae goes as follows. For each event, I calculate the $P(\ell_i,\sigma_1,\ell_0)$ for a sequence of twenty ℓ_0's which brackets the anticipated result. The logarithm of $P(\ell_i,\sigma_1,\ell_0)$ is then added to a running total kept separately for each ℓ_0. When all events have been included, the table of $\ln(\mathcal{L})$ vs. ℓ_0 represents the functional dependence of $\mathcal{L}$ on ℓ_0. The local maximum yields the best estimate of ℓ_0; variation of 1/2 in corresponds to a one σ variation in ℓ_0 [25]. A parabolic fit to the peak region, in conjunction with these facts, yields the mean path length and its error.

The reliability of this procedure has been checked against Monte Carlo generated data. The Monte Carlo includes accurate representation of VC and DC resolutions, multiple coulomb scattering in the beam pipe, chamber wires, and VC/DC interface, nuclear scattering and absorption

in the beam pipe, pion and kaon decay, photon conversions, and even a duplication of dead wire patterns in the two chambers. Two data sets of 20K tau's were generated, one with the canonical lifetime, and the other with zero lifetime. Additional information available in the MC data allows the calculation of the true unsmeared flight path in each event, and thus the true average in each sample. Each data set was subjected to the complete analysis procedure, culminating in the appropriate maximum likelihood analysis. The path length distributions for passing events are shown in figs. 4.14a and 4.14b. The results of the maximum likelihood fits were:

lifetime	number used	$\langle l \rangle$ from MC	$\langle l \rangle$ from max like
0 sec	1478	0.0μ	28±20 μ
2.8E-13 sec	1591	612μ	597±22 μ

In both cases, the measured lifetime agrees with expectations to within the statistical error.

The width of the zero lifetime distribution arises solely out of the experimental errors; fig. 4.14a is therefore a Monte Carlo representation of the expected "resolution function". We can check our understanding of the resolution by recasting this distribution in units of the expected error. Fig. 4.15 is the distribution of l/σ_l; it is nicely gaussian, with a width of 0.97±.02. This confirms that, in the Monte Carlo anyway, the tracking vertexing, and path length calculating does yield a gaussian error which is well represented by the calculated σ_l.

a)

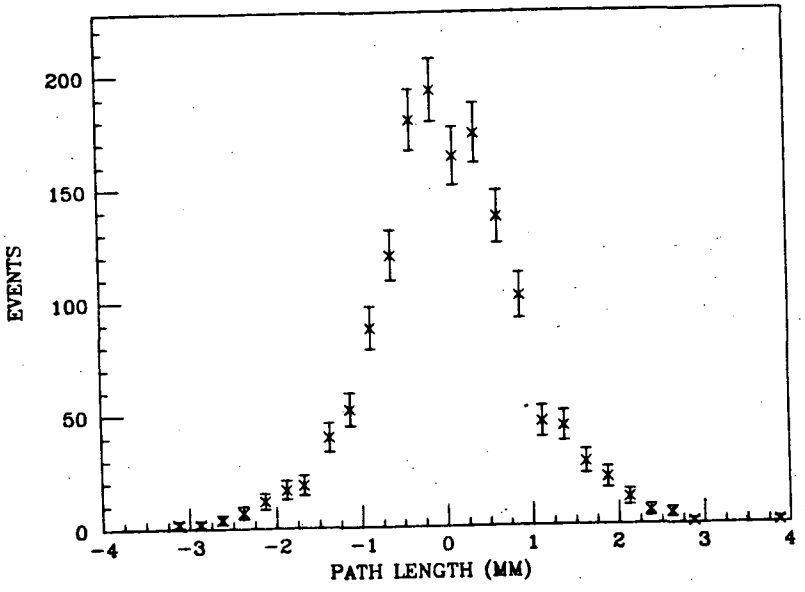

b)

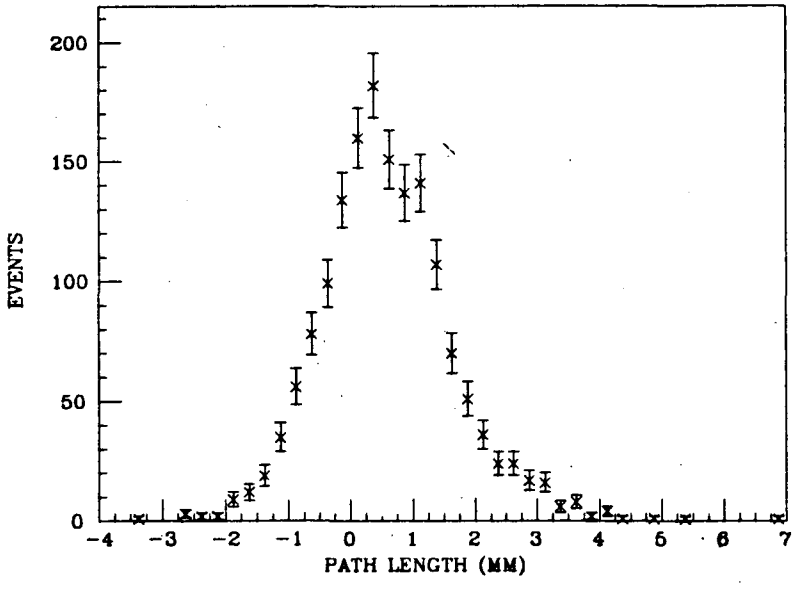

Fig. 4.14 Path length distributions for Monte Carlo tau events
a) with zero lifetime
b) with the canonical lifetime

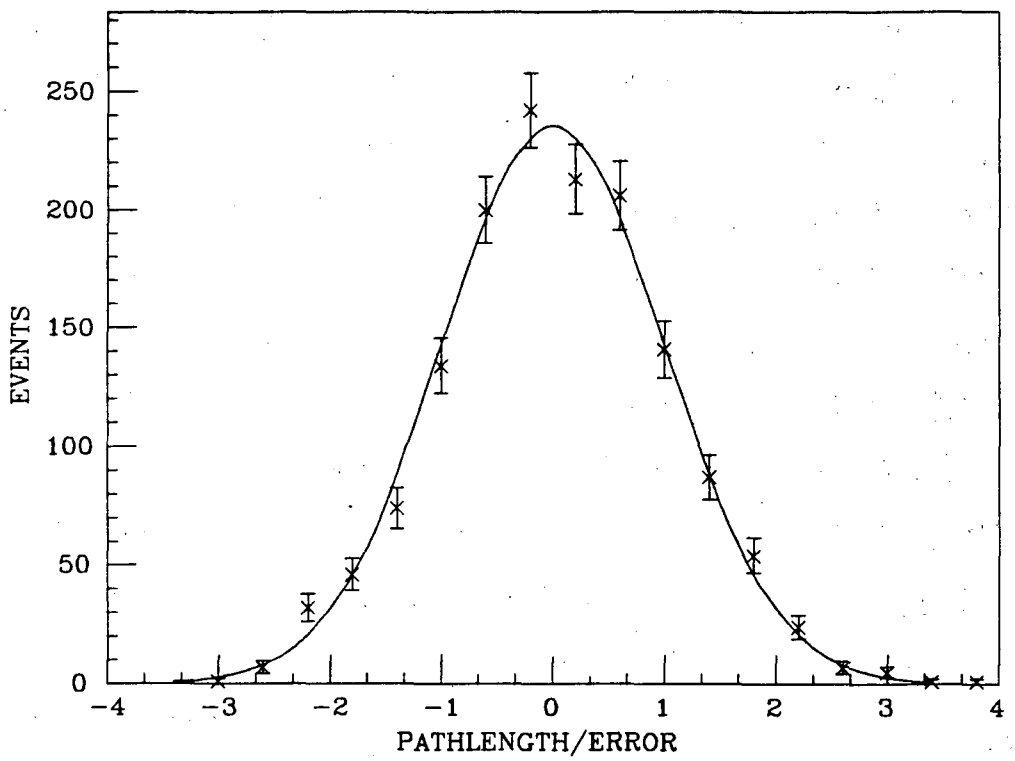

Fig. 4.15 Path lengths in the zero lifetime MC tau sample in units of the path length error

4.5 The mean tau path length. A caveat

The maximum likelihood procedure for finite lifetime is now applied to the distribution of tau flight paths in fig. 4.13. The likelihood function which results is shown in fig. 4.16. A parabolic fit to the peak gives

$$\langle \ell_\tau \rangle = 658 \pm 48 \ \mu$$

This result is somewhat greater than the mean quoted in sec 4.3 and significantly closer to the expected value of 680 μ. But before it is carved into stone, it is important to note one weak spot in the analysis procedure: the maximum likelihood machinery examines the shape of the experimental distribution, and draws a conclusion from this shape in conjunction with the calculated σ_1's. The calculation of these quantities includes contributions from every source of error that could be anticipated, and the Monte Carlo data has shown that when we understand the errors going in, we understand the error coming out. Nevertheless, it is possible, that there exist additional unanticipated contributions to the error, and the bhaba miss distance study of sec. 3.6 certainly supports the conjecture. This possibility is addressed in detail in the following chapter.

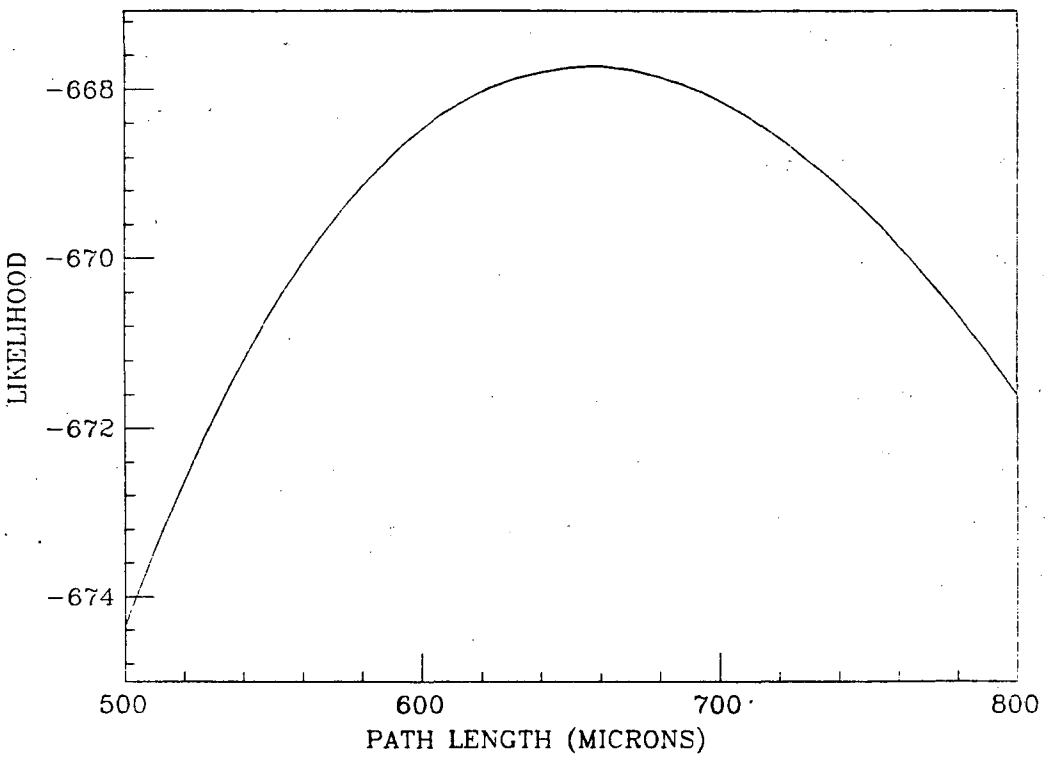

Fig. 4.16 Likelihood vs. mean tau pathlength

5. SYSTEMATICS WITH THE HADRON CONTROL SAMPLE

5.1 Introduction

Although the mean path length analysis has been checked against the Monte Carlo data sets, the Monte Carlo is, unfortunately, always part of the controversy of whether art imitates life. In particular, as emphasized in sec. 4.5, the Monte Carlo checks provide only limited confidence in our understanding of the actual experimental resolution. It is therefore necessary to check the performance of the analysis procedure against some control data sample.

It is clear that this control sample should, where possible, reproduce the essential qualities of the 3 prong tau events. To this end, I construct a sample of 'pseudo-tau' events by judicious selection of triplets from multiprong hadronic events. In the limit of zero lifetime charm and bottom quarks, this sample provides a known lifetime (0.0 sec) against which we can calibrate.

5.2 Event selection

A first set of cuts simply checks for a hadronic multiprong of reasonable quality:

$N_{\text{charged tracks}} \geq 7$

Event vertex within 1.0 cm of XYZIR in the xy plane

Event vertex within 5.0 cm of XYZIR along the z direction

χ^2 of event vertex $\leq$ 30.0 per degree of freedom

10.0 Gev/c $\leq$ total $P_{\text{charged}} \leq$ 30.0 Gev/c

The first cut removes the background from tau's. The other cuts remove background from beam burps, beam gas scattering, and other miscellaneous sources of junk events.

Passing events were retracked with ADDTC as per the tau's, except VC tracking errors were increased by a factor of 1.3. This error enhancement was found from a study of track χ^2 similar to that discussed in sec. 4.2; it is larger than the enhancement found for tau's, and presumably reflects the increased tracking difficulties in the dense hadronic events.

The retracked events were then subjected to simple track quality cuts based on distance of closest approach to the beam center (DCA) and track momentum (P_{tr}):

$$\text{DCA in xy} \leq 2.0 \text{ cm}$$

$$\text{DCA in z} \leq 5.0 \text{ cm}$$

$$P_{tr} \leq 0.400 \text{ Gev/c}$$

The rationale behind these cuts is much as discussed in the tau analysis.

Tracks from K^0 or Λ decay will contribute anomalously large path lengths to the control sample lifetime; tracks which combine with any other oppositely charged track to give a K^0 or Λ mass were therefore disqualified. (The K^0 calculation assumed pion masses; both combinations of p and π masses were tried in the Λ case.)

To accurately model the expected resolution, the control must resemble real tau's in the distribution of momentum and opening angle. The former is complicated by the softness of the momentum spectrum in hadrons compared to tau's. The strategy for finding momentous pseudo-tau's will be to order passing tracks in terms of their momenta, and look for the three highest momentum tracks which satisfy the following:

$$3.0 \text{ Gev/c} \leq P_{3prong} \leq 15.0 \text{ Gev/c}$$

$$3 \text{ prong opening angle} \leq 0.70 \text{ rd}$$

$$P_{3prong}/M_{3prong} \geq 4.0$$

Suffice it to say that the low end of the first cut above is difficult to satisfy unless we focus on the highest momentum tracks in the event. The ratio in the last cut corresponds to the purely kinematic quantity $\gamma\beta$; it stresses the velocity dependence of σ_1, as opposed to opening angles. Plots of these quantities for tau's and pseudo-tau's are shown in figs 5.1 to 5.3. In spite of the softness of the effective velocity distribution of pseudo-tau's, the momentum and opening angle distributions turn out to be roughly well matched.

5.3 Preliminary control lifetime. B and C contamination.

The control resulting from the above cuts was subjected to the complete tau analysis, including all quality cuts. The distribution of σ_1's is shown in fig. 5.4; it is slightly more concentrated at smaller errors, but reproduces the real tau's rather well. The distribution of path lengths is shown in fig. 5.5. It peaks at zero, but shows a slight bias to positive lifetimes. Avoiding, for the moment, the

a)

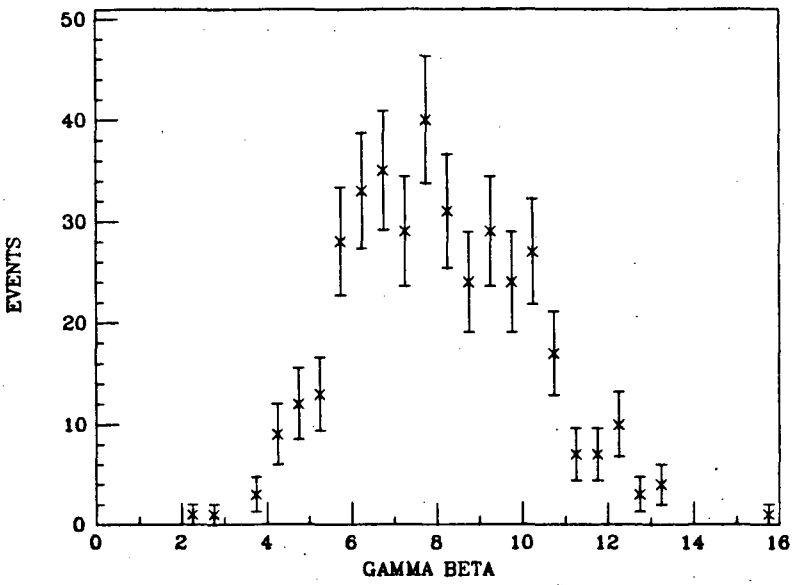

b)

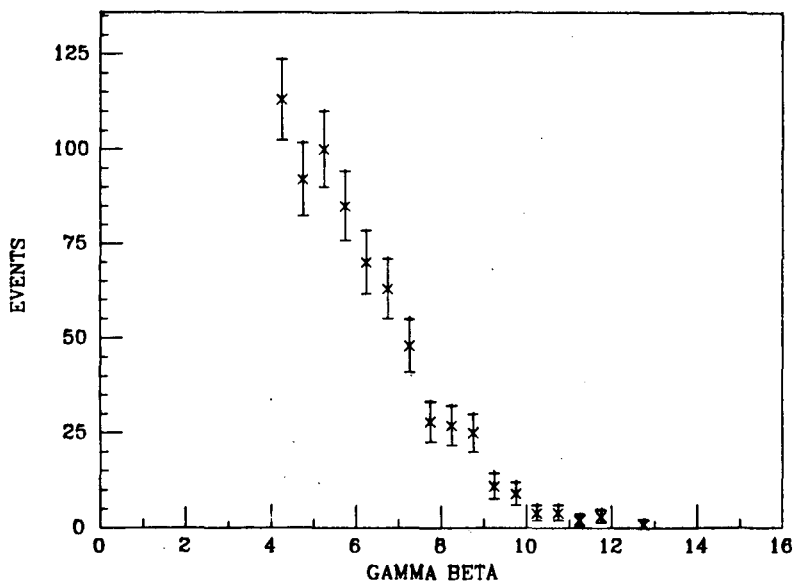

Fig. 5.1 Gamma beta
a) for real 3 prong tau decays
b) for pseudo tau's

a)

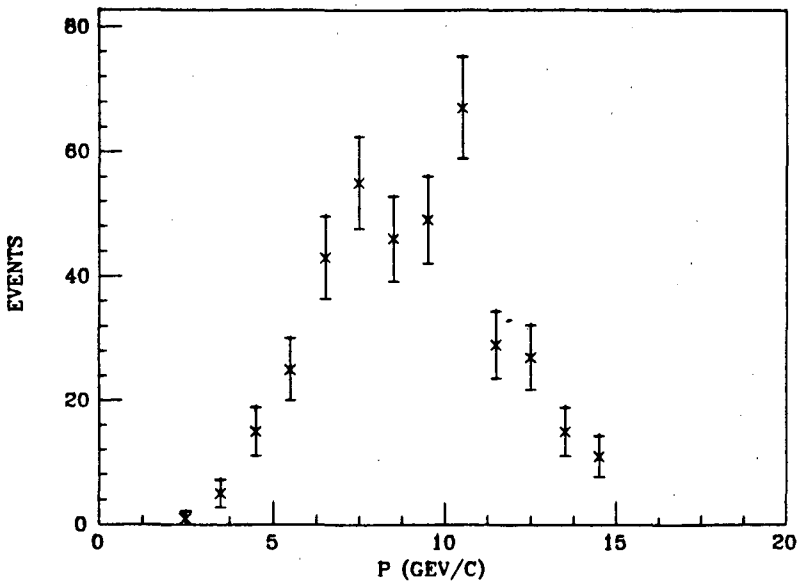

b)

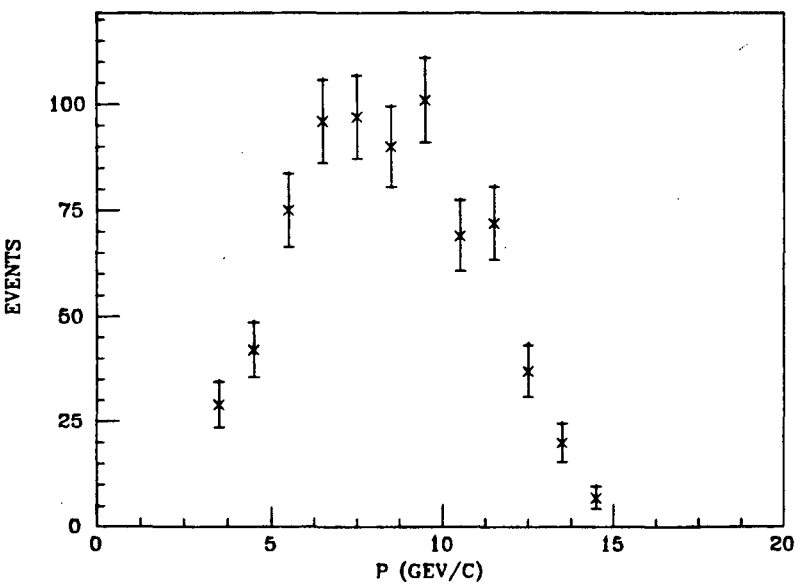

Fig. 5.2 Momentum of the 3 prong system
a) for real tau's
b) for pseudo tau's

a)

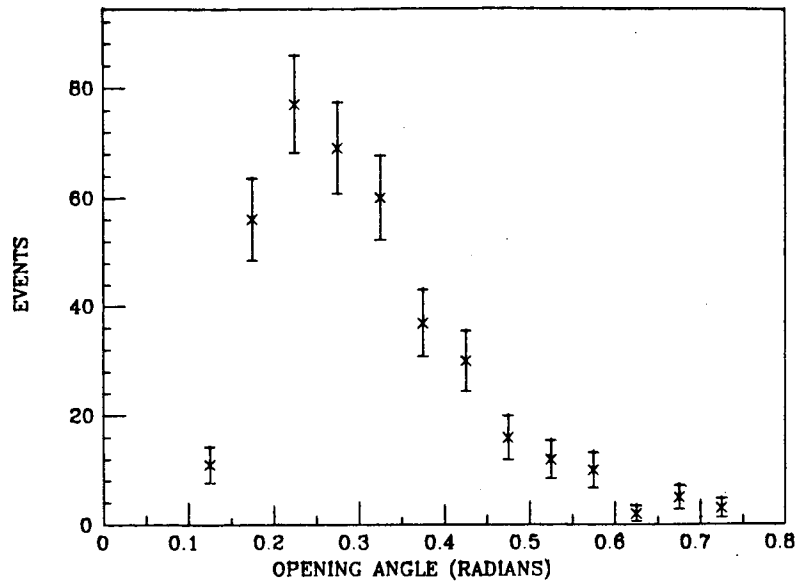

b)

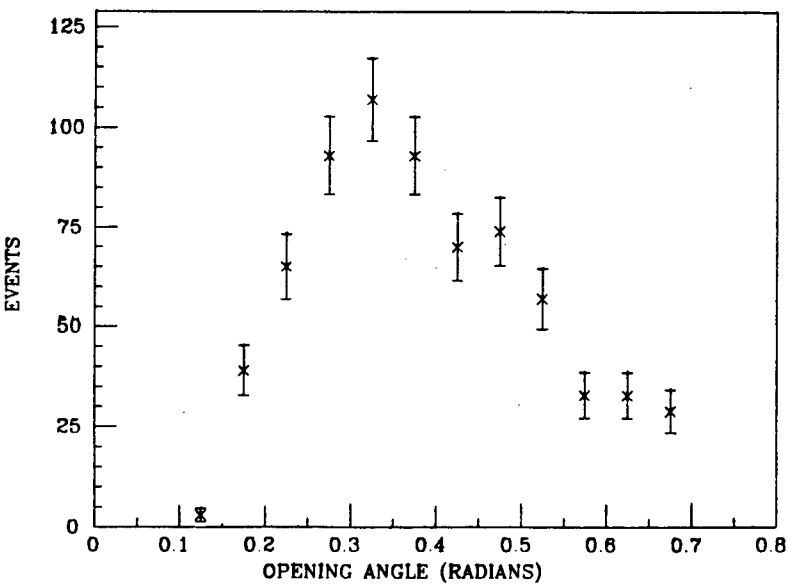

Fig. 5.3 Opening angle of the 3 prong system
a) for real tau's
b) for pseudo tau's

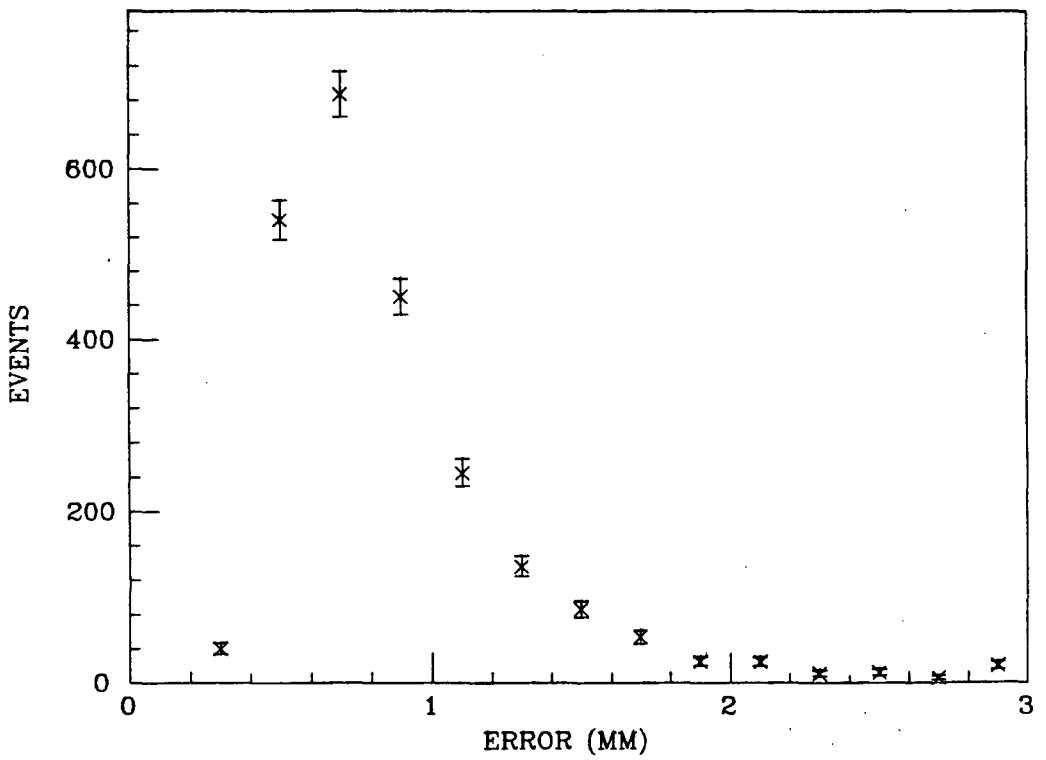

Fig. 5.4 Path length error in the data control sample

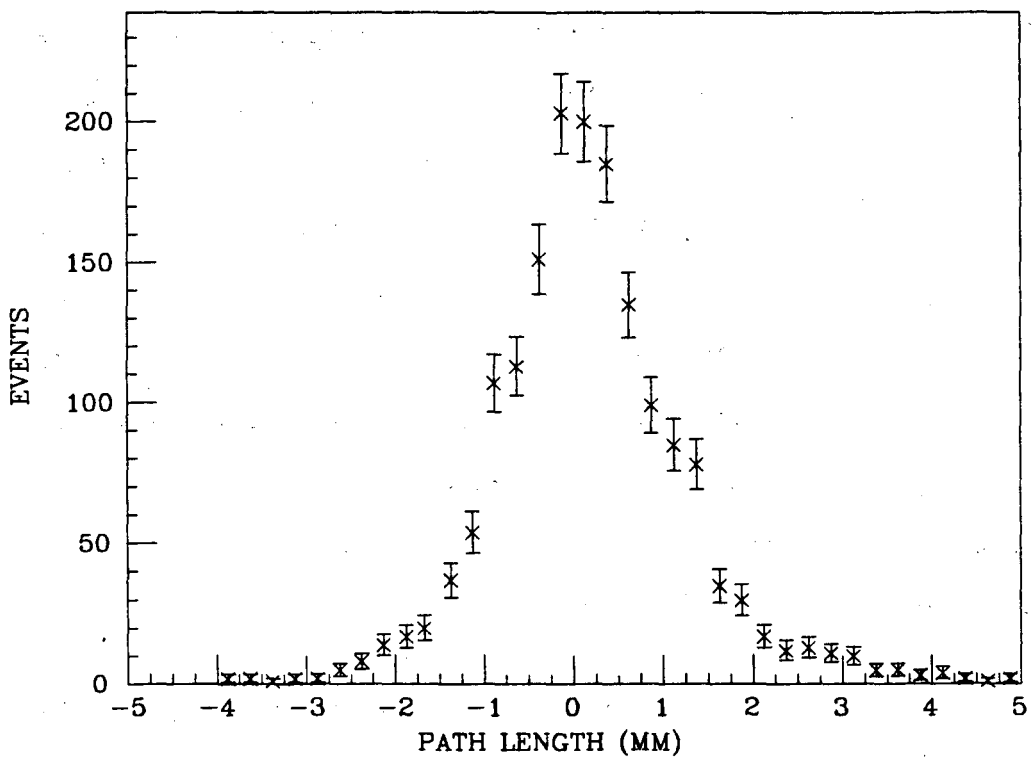

Fig. 5.5 Path lengths in the data control sample

complications of maximum likelihood, we use a normally weighted average to find a mean path length of 192± 16 microns.

The finite mean path length is presumably due to tracks coming from the decay of particles with charm and bottom. To help elucidate this assumption, a parallel sample of pseudo-tau's was culled from the Mark II QCD Monte Carlo. The Monte Carlo uses Feynman-Field fragmentation, and includes the latest Mark II results on fragmentation functions and heavy quark lifetimes [22,23,26]. It also utilizes all of the refinements listed in sec. 4.4. The flight path distribution from this sample is shown in fig. 5.6. It also shows a very slight tail at positive lifetimes. The weighted mean is 105±13 microns: smaller than the data, but still significantly non-zero. Is this from charm and bottom? To test, I used the MC production information to drop all but those events originating from u and d quarks. The resultant $\langle \ell \rangle$ is found to be 1±23 μ; in the MC anyway, finite lifetime for the hadron control sample <u>is</u> the result of charm and bottom.

It is now of some interest to see if the heavy quark contamination of the control sample can be reduced. To avoid the feeling of groping in the dark jet, I look for parallel effects of cuts in both the data and MC controls. One method of flagging tracks from b or c decay is to look at impact parameters. The distribution of DCAs to XYZIR is shown in fig. 5.7; a cut at 1.0 mm will eliminate gross offenders without biasing the bulk of the distribution (recall the DCA considerations of sec. 4.2) Another approach is based on the fact that b and c

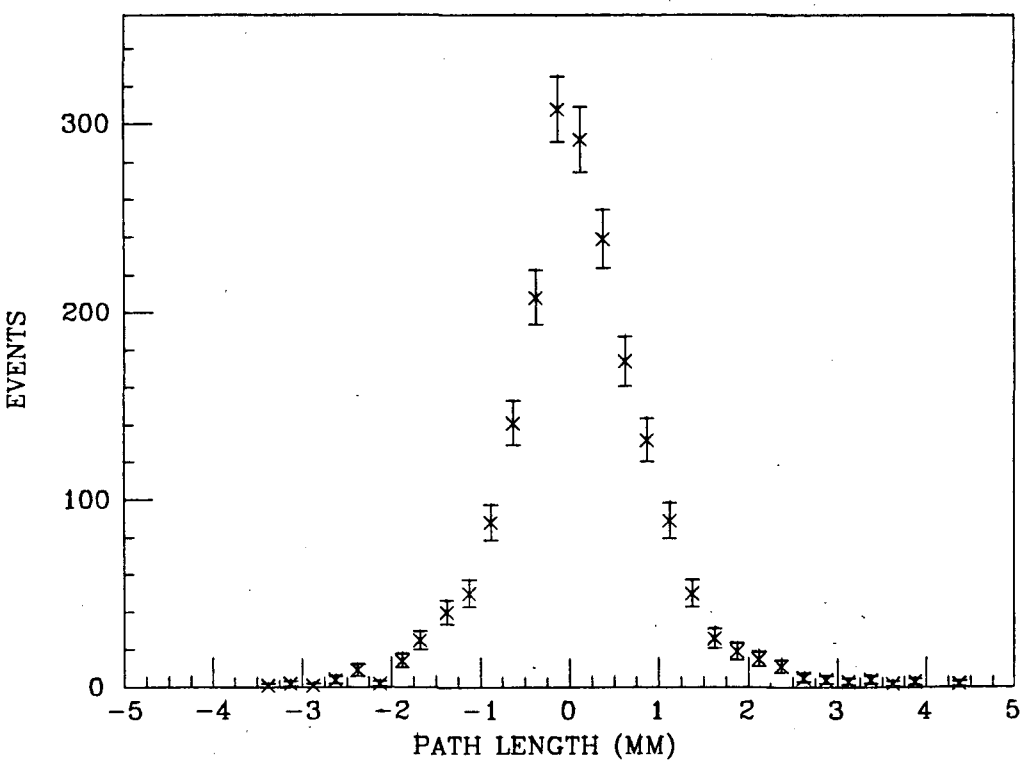

Fig. 5.6 Path lengths in the Monte Carlo control sample

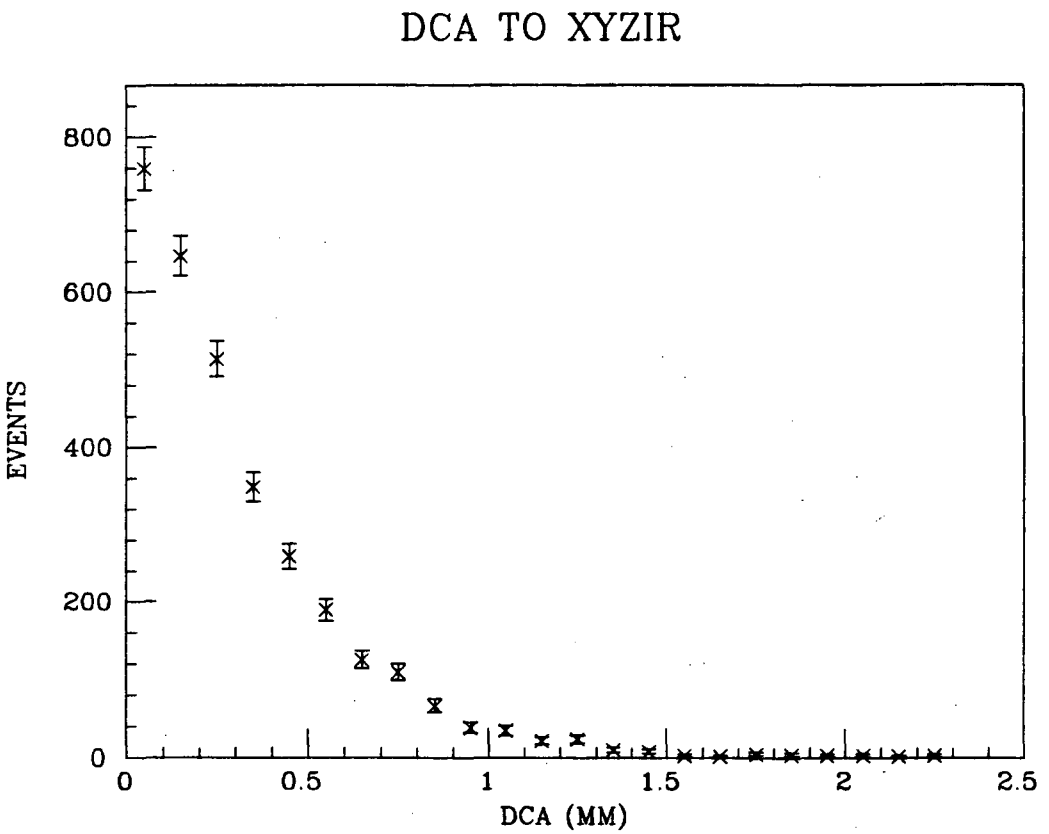

Fig. 5.7 DCA of tracks to (x_b, y_b) in the data control sample

fragmentation functions peak at high z ($z=E_{hadron}/E_{beam}$); the cut is then simply to eliminate the highest momentum track in the event (P_1). The effect of these cuts on data and MC control samples is tabulated below:

	DATA CONTROL		MC CONTROL	
cut	number	mean path (μ)	number	mean path (μ)
none	1670	192±16	1963	105±13
DCA≤1.0	1627	160±16	1937	103±13
drop P_1	887	104±23	1050	105±18
DCA + P_1	863	79±23	1036	95±18

The P_1 cut reduces the data lifetime by fully four sigma; the DCA cut has a smaller, but still significant effect. If the finite path length is truly from c and b, it seems that these simple requirements do succeed in reducing the size of this component. Unfortunately, none of this is borne out by the Monte Carlo, which shows no significant reaction to the cuts.

If the MC is correct, the discrepancy could possibly be due to some kind of tracking problem at high momentum. I have checked chisquareds, number of hits, and DCA distributions of the high momentum tracks in this sample, and found no evidence of such a problem. My suspicions lie, instead, with the Monte Carlo. The data control ℓ vs. σ_1 distri-

butions for the case of 'no cuts' and 'P_1 + DCA' are shown in figs. 5.8a and 5.8b, respectively. Fig. 5.8b indicates that the bulk of the 'P_1 + DCA' sample has ℓ between ±2.5mm, with the positive tail slightly more predominant. Fig. 5.8a shows the 'no cut' sample to have a obvious tail beyond +2.5mm. These events are presumably the origin of the efficacy of the cuts in the data. As seen in fig. 5.8c, however, the 'no cut' Monte Carlo sample does not show the strong tail beyond +2.5mm.

What is the tail in the 'no cut' sample? Fig. 5.9a is one of the data events that is dropped by the P_1 cut. The 'pseudo-tau' is the isolated 3 prong system. Track 8 has p=6.9 Gev/c, which explains why this event was dropped when the highest momentum track was excluded. The mass (including nearby neutrals) of the isolated system is 1.7 Gev, highly suggestive of D decay. Another event from the tail is shown in fig. 5.9b. The 'pseudo-tau' is the system in brackets. Track 3 is 5.7 Gev/c. The mass of the 4 prong system in the 'pseudo-tau' hemisphere is 2.1 Gev/c^2.

The presence of several other events like these in the '+2.5mm tail', and their absence from the Monte Carlo, suggests that our understanding of charm fragmentation (or at least the MC implementation of it) is might be failing at high z and low multiplicity. For the remainder of our work with the control sample, I shall assume that the 'P_1+DCA' cut <u>is</u> actually removing charm and bottom, and adopt this data set as the standard control sample.

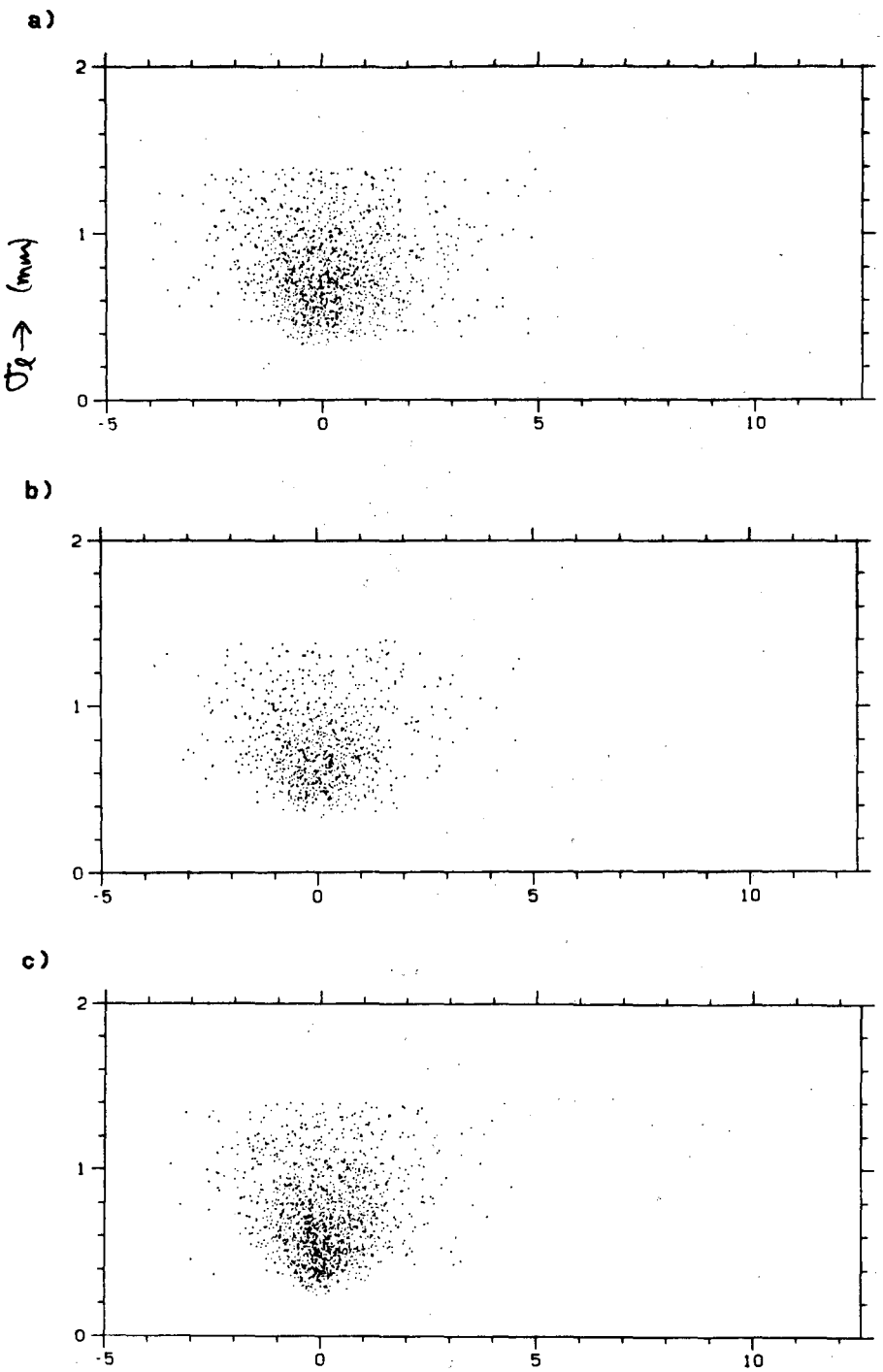

Fig. 5.8 Path length vs path length error in:
a) data control sample with no cuts
b) data control sample with DCA and P_t cuts
c) Monte Carlo control sample with no cuts

a)

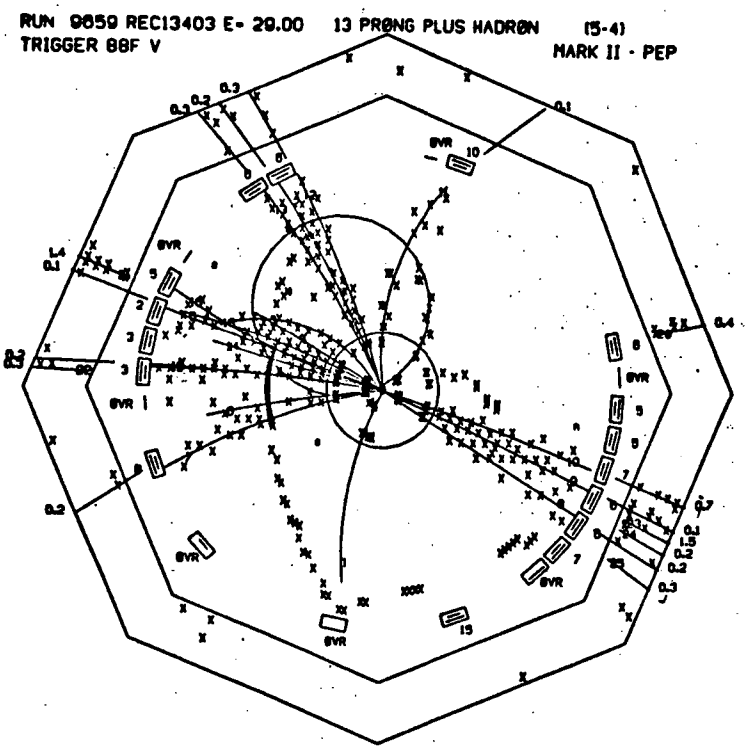

b)

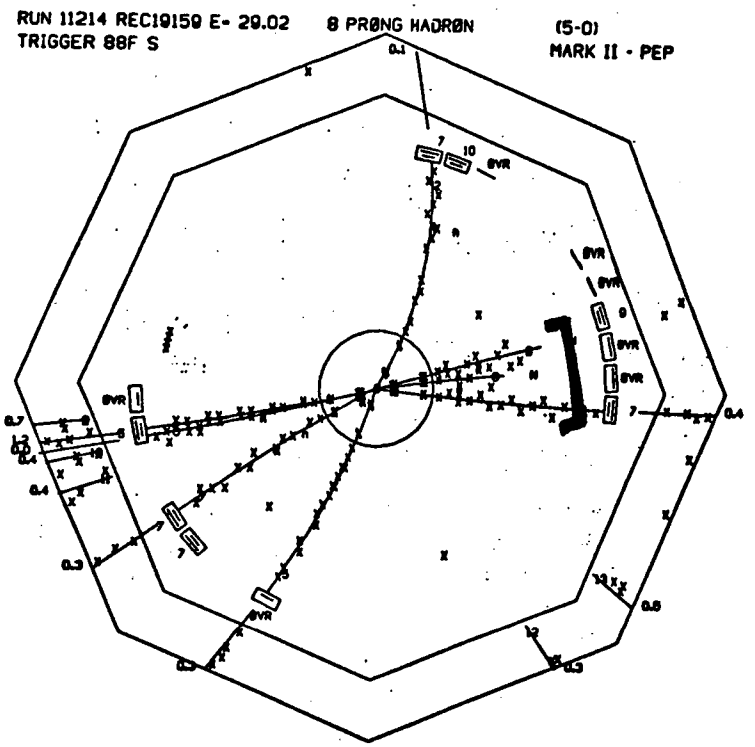

Fig. 5.9 Illustrative control sample events with 'long' lifetimes

5.4 Check of the maximum likelihood result. Correction to resolution

I now utilize the control data sample as a check on path length calculating machinery. Using the 'zero lifetime' likelihood function, the mean path length in the sample is found to be 213±23 μ. This compares very unfavorably with the weighted mean of 79±23 μ. Since the mean has to be correct in the limit of this large statistic, a bias must exist in the other procedure.

To uncover the source of this bias, consider, first, the short lifetime likelihood function:

$$P(l_i, l_o, \sigma_{l_i}) = \frac{1}{\sqrt{2\pi(\sigma_{l_i}^2 + l_o^2)}} \; e^{-\frac{(l_i - l_o)^2}{2(\sigma_{l_i}^2 + l_o^2)}}$$

The maximum likelihood procedure is find the l_o which gives the extremum:

$$\frac{\partial}{\partial l_o} \sum_i \ln\left[P(l_i, l_o, \sigma_{l_i})\right] = 0$$

If we assume, for the moment, that the error is the same in every event, we find, after some algebra, an implicit relation for l_o:

$$l_o = \frac{\sigma_l^2 \sum_i l_i - N l_o^3 - l_o^2 \sum_i l_i}{2N\sigma_l^2 - \sum_i l_i^2}$$

In our case, $\sigma_l >> l_o$, and we can approximate:

$$l_o \cong \frac{\sigma_l^2 \sum_i l_i}{2N\sigma_l^2 - \sum_i l_i^2}$$

In the denominator of this expression, we find a comparison between the

experimental width $\sum \ell_i^2$ and the calculated error σ_l. If, as discussed at the end of chapter 4, there exist unanticipated contributions to the experimental resolution, the calculated σ_l's will be too small in comparison to the experimental width; this expression shows that such an error will produce a result which is too large, as we observe. Assuming that the weighted mean is correct, we can use this expression to predict that our calculated σ_l's are too small by a factor of approximately 1.3.

To verify this prediction, we measured the path length in units of its error, as already done for the Monte Carlo data in sec 4.4. We assume that the mean path length is 80 μ and plot for the data the distribution of the quantity

$$(\ell - 80\mu)/\sigma_l$$

The width of the resultant distribution was 1.31±0.03, as expected.

As an independent check of our estimates of the size of this rescaling, I modified the maximum likelihood machinery to fit <u>both</u> the lifetime and the scale of the error, which I shall denote as R. Running on the control sample I found a best fit of:

$$\langle \ell \rangle = 84 \pm 30\ \mu \text{ with } R = 1.30$$

The size of the scaling is just as predicted, and the mean path length is consistent with that given by the weighted mean.

The use of this fitting procedure on the Monte Carlo control sample provides some insight into the origin of this broadened error. The results from the MC control sample were:

$\langle \ell \rangle$ from weighted mean: $95 \pm 18\ \mu$

$\langle \ell \rangle$ from maximum likelihood: $98 \pm 21\ \mu$ with R=1.14

The maximum likelihood result indicates that errors in the Monte Carlo should be increased by 14%. This contradicts the earlier work with the tau Monte Carlo, which demonstrated that the σ_l's in the Monte Carlo were correct. The origin of this contradiction becomes clear if we rerun on the MC control sample using the Monte Carlo production information, as before, to omit all but u and d events. In this case, we find:

$\langle \ell \rangle$ from weighted mean: $1 \pm 19\ \mu$

$\langle \ell \rangle$ from maximum likelihood: $2 \pm 21\ \mu$ with R=1.00

The mysterious broadening in the Monte Carlo control occurs only when charm and bottom pollute the sample. I believe this is due to the random way in which tracks from charm and bottom get combined into the pseudo- tau's. In the limit of zero error, the distribution of path lengths from these vertices will not be exponential, as the likelihood functions assume. This mistake appears as an increase in our width.

Recall that the data control sample had apparent errors 30% larger than anticipated. If we assume that 14% of this is due to this effect

seen in the Monte Carlo, we anticipate that real data contains a residual 16% broadening due to unknown errors. The source of these unknowns is presumably the combination of small errors from a host of sources. These would include errant wire positions, field irregularities in regions with high voltage problems, bad calibrations, bad beam positions and so on.

The strategy for dealing with this additional error will be phenomenological in nature. I accept that it exists, and I assume that it can be treated by a uniform rescaling of the calculated error. By using the maximum likelihood technique to fit both the path length and the scale of the error, we can then account, in an average way, for all of the unknown foibles in the data. This is the procedure that will now be applied to the distribution of tau flight paths.

6. MEASUREMENT OF THE TAU LIFETIME

6.1 Maximum likelihood result

The study of the hadronic control sample indicates that the calculated σ_l's are underestimated, but that the sensitivity to this error can actually be removed by fitting for both the mean path length and the relative scale of the error. This strategy is now applied to the tau flight path distribution of fig. 4.12. The result is

$$\langle l \rangle = 621 \pm 52\ \mu \text{ with } R = 1.13 \pm .05$$

The error on the path length includes the error in R. The fitted scaling is consistent with the 16% expected from the argument at the end of sec. 5.4. Recall that when fit with no rescaling for σ_l, we found $\langle \ell \rangle = 658 \pm 48\ \mu$; allowing the error to vary in the fit reduces the measured value by about 5%. This is at the limit of statistical significance, but well supported by the control sample study.

The graphical success of this fit is shown in fig 6.1. The smooth curve is constructed by numerically convoluting an exponential of $\langle \ell \rangle = 620\ \mu$ with a resolution function representing the normalized superposition of 423 gaussians, one for each event. The width of the gaussian associated with a given event was taken to be $\sigma_l \times 1.13$. The curve describes the data very nicely.

As another check on the error fitting procedure, I tried fitting not a scale, but an extra error to be added in quadrature to the σ_l's. This more accurately models the situation where the mystery error

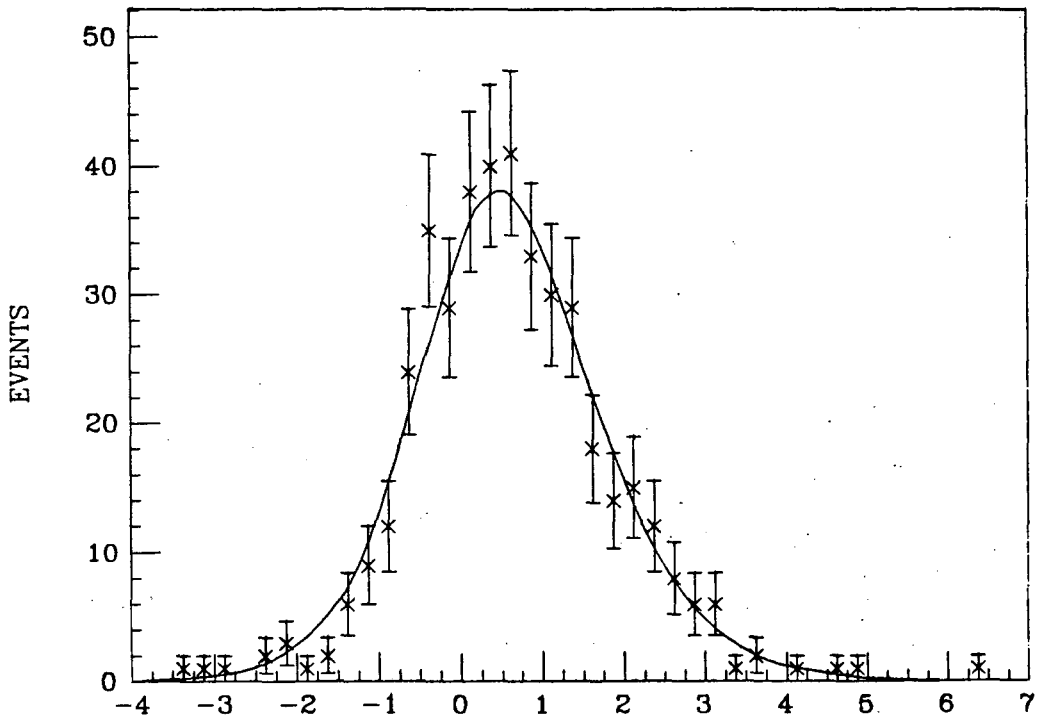

Fig. 6.1 Fit of measured path length function to data

arises from a source independent of σ_l. In this case, we found

$$\langle \ell \rangle = 628 \pm 52\ \mu \quad \text{with } \sigma_{extra} = 400\mu$$

The $\langle \sigma_l \rangle$ in this sample is 891μ. Note that if the real error is the sum in quadrature of $\langle \sigma_l \rangle$ and σ_{extra}, this result predicts an R of

$$\text{sqrt}(891^2+400^2)/891 = 1.10$$

So, both the path length and average increase in the error are in very good agreement with the results found by the scaling technique.

For the final value, I shall use the scaling result, and assign as a systematic error the 7μ difference between these two techniques.

6.2 Backgrounds

The main sources of background to the tau sample used in this analysis have been discussed in sec. 5.1. They are: low multiplicity hadrons, tau pairs from $\gamma\gamma$ collisions, and radiative bhaba and dimuon events. As all of these give a "3 prong flight path" less than that of tau's produced in one photon annihilation, the presence of a small background component will shift the measured path length down by some amount. The size of this background component, as well as the expected shift in the measured flight path, can be evaluated with the help of the Monte Carlo.

6.2.1 Relative efficiencies

The basic strategy of the background estimate is to generate a sample of MC background with known luminosity, and then see how many events pass the cuts in the analysis program. A correct normalization

to the known luminosity of the data then requires a calibration: we must measure the relative efficiency for event finding in real data vs. Monte Carlo. With the measured tau branching ratios of 86% into 1 prong, and 14% into 3 prong [16], I calculate the number of 4 prong and 6 prong topologies expected in the full 134 pb^{-1} sample. Using the number of each topology which passes all cuts, I find the efficiency of finding both the 4 and 6 prong tau pairs in the data to be

$$\epsilon_{data} = 10\%$$

with negligible error. Note that the basic similarity of the two topologies is consistent with finding the same efficiency for each.

To measure the efficiency for finding tau's in the MC data, I use this same technique on the nominal lifetime tau Monte Carlo data discussed in sec. 4.4. In this case, the known branching ratios in the MC are used to calculate the number of events expected. Comparing to the throughput, I find the efficiency of finding MC tau's to be 18.3% for 4 prongs and 14.5% for 6 prongs. Since these numbers are expected to be the same, I impose this condition, concluding that the MC efficiency for both topologies is

$$\epsilon_{mc} = 16.0 \pm 2.0\ \%$$

Comparing this to the value found for real data, we must conclude that data tau's are found less efficiently by relative factor of

$$\epsilon_{data}/\epsilon_{mc} = 0.62 \pm .08$$

As we have already seen that the data are degraded with respect to the MC in several ways, the direction of this result is quite sensible. I shall assume that this factor applies equally to each of the back-

grounds that I shall examine.

6.2.2 Hadronic background

The first such sample is low multiplicity hadrons. On an equivalent luminosity of 159 pb^{-1}, the tau program found 30 events which passed all cuts. The expected contamination in the data is then

$$\frac{134}{159} \times \frac{30}{423} \times (0.62 \pm .08) \simeq (4.0 \pm 0.5)\%$$

In this case, there is also the complication of knowing whether the hadronic Monte Carlo correctly reproduces the data in the low multiplicity region. To test this in a tau free regime, I ran the analysis program on the full data set and the hadronic MC with the 3 prong mass requirements set to

$$2.0\ \text{Gev/c}^2 \leq M_{3\pi} \leq 4.0\ \text{Gev/c}^2$$

$$2.0\ \text{Gev/c}^2 \leq M_{3\pi+\text{neutrals}} \leq 4.0\ \text{Gev/c}^2$$

The results of this search are summarized below for each topology:

N_{prong}	found in MC	found in data
6	1	0
4	6	3

The statistics are poor, but when combined with the efficiency factor, the result indicates that the MC is in reasonable agreement with the data. To reflect the poor statistical precision of this check, however, I assign a 50% uncertainty to the predicted amount of the hadron contamination.

6.2.3 $\gamma\gamma$ tau production

The estimate of contamination from $\gamma\gamma$ tau pair production is somewhat more straightforward. The 2γ Monte Carlo generates tau pairs from two photon collisions in the Weizacker-Williams approximation; the program integrates the differential cross section over detector acceptance: with a threshold at the mass of a tau pair, the total cross section is .089±.01 nb, where the uncertainty is due to higher order effects. Using this cross section, I calculate an expected $(1.2\pm0.1)\times10^4$ events due to this process in the 134 pb^{-1} of data. In a sample of 1.5×10^4 MC produced tau pairs,the tau analysis program found 26 events which passed all cuts. The 2γ tau contamination of the data set is then given by:

$$\frac{(1.2\pm0.1)\times10^4}{1.5\times10^4} \times \frac{26}{423} \times 0.62\pm0.08 \simeq (3.0\pm1.0)\%$$

6.2.4 Other backgrounds

The remaining backgrounds are apparently present only at the trace level. An equivalent 24 pb^{-1} of radiative bhaba MC produced no passing events. One passing event in this sample would correspond to a total of five in the tau data set. Assuming a mean lifetime of zero, the presence of these events would lower the measured flight path by 1%. An equivalent 95 pb^{-1} of radiative dimuons also produced no passing events; I conclude that background from this source is minimal. In one final check, an equivalent $25pb^{-1}$ of 2γ produced hadrons also gave no passing events. The worst case consequences here are identical to

those for radiative bhabas.

6.2.5 Background correction

The effect of the hadron and 2γ tau backgrounds are difficult to evaluate in vitro: these events have σ_1's distributed according to their own momentum spectra and opening angle distributions, and are therefore weighted with respect to the tau sample in a non-trivial way. Fortunately, the situation can be modeled with the Monte Carlo. The procedure is to measure the mean path length of a MC tau sample, then mix in the passing MC background events in the appropriate ratios and observe the net change in the path length. To maximize the statistical precision, the size of the MC tau sample was chosen so that most of the MC background events could be used. The effect of adding the hadron and 2γ background was to lower the mean path length by 31μ. Assuming the effect is linear with the size of the contamination, the uncertainties in the background fraction indicate the error on this number is 21μ.

6.3 Systematic errors

The main systematic uncertainty remaining in this measurement is the magnitude of offset, if any, in the experimental resolution function. That is: for a sample originating at the origin, would this procedure yield zero lifetime? This issue is best addressed by the hadron control sample. Unfortunately, the complicating contamination of finite pathlengths originating in charm and bottom decays means that the result can only be checked against the Monte Carlo, thereby introducing

a host of model dependent effects. One such effect is the different response of the data and MC control samples to the cuts discussed in sec. 5.3. I shall assume, as outlined there, that this difference is due to a small inaccuracy in the Monte Carlo, and that the sensitivity of the analysis to this inaccuracy is diminished by the application of the 'P1+DCA' cut to the data. In this case, the important remaining model dependence lies in the MC values of the D^0 and D^+ lifetimes, the $D^0/D+$ ratio, and the mean B lifetime. Reasonable independent variations in these parameters were found to change the mean pathlength of the MC control sample by 15 to 20 microns in each case. Adding the variations in quadrature, I find that the total error from these effects is approximately 30 microns.

Turning, now, to the actual comparison of the results, the last line of the table on page 91 indicates that, in fact, the mean pathlengths of the data and MC control samples agree to within the statistical errors. I take this to indicate that the potential offset error in the analysis is bounded from above by the error in this comparison, namely, the sum in quadrature of the statistical errors and the possible error from model dependence. All told, this gives an estimated offset error of 42μ.

The magnitudes of other potential errors are checked by varying certain key assumptions. On the basis of a slightly different path length found using ORCALC beam positions, I estimate a maximum error due to errant beam positions of 15μ. Reasonable variations in the σ_1 cut pro-

duced maximum variations in the mean path length of 15μ. Reasonable variations in the χ^2 cuts produced maximum variations in the mean path length of 20μ. A stricter requirement on the number of hits in the VC, demanding 3 hits in the inner band and 2 in the outer for each track, moved the mean path length up by 15μ.

The effect of assuming that the 3 prong exactly follows the tau direction was studied via Monte Carlo, where the true tau direction is available through the MC production information. The net difference in $\langle \ell \rangle$ when the true direction is substituted for the 3 prong direction is 2μ.

Adding all of these contributions in quadrature, and remembering to include the error in the background estimate, as well as the small uncertainty assigned to the scale fitting procedure, I arrive at a net systematic error of 57μ.

6.4 The tau lifetime

Including the background correction of sec. 6.2 the final result for the tau path length is

$$\langle \ell \rangle = 652 \pm 55 \pm 58 \ \mu.$$

The background correction scales the mean path length up by about 5%; the statistical error has correspondingly been increased by the same amount. Radiative corrections diminish the mean energy of the tau's slightly with respect to the beam energy; the tau MC puts the mean tau energy at 13.88 Gev, giving a tau γ of 7.78. The tau lifetime is then

given to be

$$\tau_{tau}=(2.80\pm0.24\pm0.25)\times10^{-13}\ \text{sec.}$$

Recall that the theoretical prediction for the lifetime is $(2.82\pm0.18)\times10^{-13}$ sec. If we assume a massless tau neutrino, this result implies exact μ-τ universality, within the errors. Combining in quadrature the errors of both the experimental and theoretical values, the precision of this statement is about 7%.

If we assume the tau coupling is universal, and that deviation from canonical lifetime is due to a massive tau neutrino, eqn. 1.4 allows a limit to be placed on the neutrino's mass. Combining the experimental statistical and systematic error in quadrature, the 2σ upper limit on the lifetime is 3.48×10^{-13} sec. This gives a 95% confidence limit of

$$M\nu_\tau \leq 275\ \text{Mev}/c^2$$

This result has been superseded by the new Mark II limit discussed in chapter 1; it is, nevertheless, a striking measure of the precision of the lifetime measurement.

If we assume that the tau neutrino is massive, but very light, and that the tau coupling is universal, a long lifetime could be the result of mixing with a fourth generation. In the parameterization described in sec.1.1, the two sigma upper limit on the lifetime would imply a mixing angle given with 95% confidence to be

$$\sin\theta \leq 0.4$$

6.5 Conclusion

We have installed a high resolution vertex detector in the Mark II at PEP, and used this detector in a precision measurement of the lifetime of the tau lepton. The result is

$$\tau_\tau = (2.80 \pm .24 \pm 0.25) \times 10^{-13} \text{ sec.}$$

where the first error is statistical, and the second is systematic. This result is consistent with e-μ-τ universality, and the prediction of the Weinberg-Salam model of the weak and electromagnetic interactions.

APPENDIX A. CALCULATION OF GEOMETRICAL CONSTANTS

A.1 The general technique

Recall, from sec. 3.2, that the basic x^2 central to all tracking is

$$\chi^2 = \sum_i \frac{(d_i^{meas} - d_i(\alpha_\mu))^2}{\sigma_i^2}$$

where α_μ are the track parameters, σ is the resolution of the drift time measurement, and d^{meas} and $d(\alpha)$ are the measured and fitted distances of closest approach. The sum is understood to run over all hits associated with a given track.

Let $\alpha_{\mu 0}$ be the track parameters from a previous iteration, and let the fitted distance of closest approach of this track to the ith wire be given by d_{i0}. Furthermore, let

$$G_{\mu\nu} \equiv \sum_i \frac{1}{\sigma_i^2} \frac{\partial d_i}{\partial \alpha_\mu} \frac{\partial d_i}{\partial \alpha_\nu} \qquad (A.1)$$

$$Y_\mu \equiv \sum_i \frac{(d_{0i} - d_i^{meas})}{\sigma_i^2} \frac{\partial d_i}{\partial \alpha_\mu} \qquad (A.2)$$

It can then be shown [30] that in the next iteration, the linearized x^2 is minimized by a new set of α_μ such that

$$\Delta\alpha_\mu = \alpha_\mu - \alpha_{\mu 0} = -\sum_\nu G^{-1}_{\mu\nu} Y_\nu \qquad (A.3)$$

$G_{\mu\nu}^{-1}$ is, in fact, just the error matrix of the fitted track. In addition, the track x^2 after this iteration is given to good approximation

by

$$\chi^2 = \sum_i \frac{(d_i^{meas} - d_{oi})^2}{\sigma_i^2} + \sum_{\nu=1}^{5} Y_\nu \Delta\alpha_\nu \qquad (A.4)$$

Let the geometric parameters relating the two chambers be some β_μ. They will be found by minimizing this χ^2 with respect to β_μ for a large ensemble of tracks. This form of the χ^2 is necessary because the track parameters themselves will depend on the geometry, and must be explicitly included if the procedure is to converge.

The algorithm will require the first and second derivatives with respect to β. The first derivative of the collective χ^2 is

$$\frac{\partial \chi^2}{\partial \beta_\mu} = \sum_{j=1}^{N} \left[2 \sum_i \frac{d_i^o - d_i^{meas}}{\sigma_i^2} \frac{\partial d_i^o}{\partial \beta_\mu} + \sum_{\lambda=1}^{5} \left(\frac{\partial \alpha_\lambda}{\partial \beta_\mu} Y_\lambda + \Delta\alpha_\lambda \frac{\partial Y_\lambda}{\partial \beta_\mu} \right) \right] \qquad (A.5)$$

where N is the total number of tracks in the ensemble. Assuming that the track errors are insensitive to small geometrical offsets, the substitution of eqn. A.3 and its derivative into the second term of the above gives

$$\frac{\partial \chi^2}{\partial \beta_\mu} = \sum_{j=1}^{N} \left[2 \sum_i \frac{d_i^o - d_i^{meas}}{\sigma_i^2} \frac{\partial d_i^o}{\partial \beta_\mu} + 2 \sum_{\lambda=1}^{5} \Delta\alpha_\lambda \frac{\partial Y_\lambda}{\partial \beta_\mu} \right]$$

Substituting the derivative of eqn. A.2 then gives

$$\frac{\partial \chi^2}{\partial \beta_\mu} = 2 \sum_{j=1}^{N} \left[\sum_i \frac{1}{\sigma_i^2} \frac{\partial d_i^o}{\partial \beta_\mu} \left(d_i^o - d_i^{meas} + \sum_{\lambda=1}^{5} (\alpha_\lambda - \alpha_{\lambda o}) \frac{\partial d_i}{\partial \alpha_\lambda} \right) \right] \qquad (A.6)$$

$$\equiv y_\mu$$

To find the second derivative, we differentiate again

$$\frac{\partial \chi^2}{\partial \beta_\mu \partial \beta_\nu} = 2 \sum_{j=1}^{N} \left[\sum_i \frac{1}{\sigma_i^2} \frac{\partial d_i^\circ}{\partial \beta_\mu} \left(\frac{\partial d_i^\circ}{\partial \beta_\nu} + \sum_{\lambda=1}^{5} \frac{\partial \alpha_\lambda}{\partial \beta_\nu} \frac{\partial d_i}{\partial \alpha_\lambda} \right) \right] \qquad (A.7)$$

Using eqns. A.2 and A.3, we can write

$$\frac{\partial \alpha_\lambda}{\partial \beta_\nu} = -\sum_{\gamma=1}^{5} G^{-1}_{\lambda\gamma} \frac{\partial y_\gamma}{\partial \beta_\nu} = -\sum_{\gamma=1}^{5} G^{-1}_{\lambda\gamma} \sum_i \frac{1}{\sigma_i^2} \frac{\partial d_i^\circ}{\partial \beta_\nu} \frac{\partial d_i}{\partial \alpha_\gamma}$$

Substitution into eqn. A.7 and a bit of algebra then yields

$$\frac{\partial \chi^2}{\partial \beta_\mu \partial \beta_\nu} = 2 \sum_{j=1}^{N} \left[\sum_i \frac{1}{\sigma_i^2} \frac{\partial d_i^\circ}{\partial \beta_\mu} \frac{\partial d_i^\circ}{\partial \beta_\nu} - \sum_{\lambda=1}^{5} \sum_{\gamma=1}^{5} G^{-1}_{\lambda\gamma} \sum_i \sum_k \frac{1}{\sigma_i^2} \frac{1}{\sigma_k^2} \frac{\partial d_i^\circ}{\partial \beta_\mu} \frac{\partial d_k^\circ}{\partial \beta_\nu} \frac{\partial d_i}{\partial \alpha_\lambda} \frac{\partial d_k}{\partial \alpha_\gamma} \right] \qquad (A.8)$$

$$\equiv g_{\mu\nu}$$

Now, assuming some starting values of β_{μ_0}, the best new choices will be those such that

$$\left. \frac{\partial \chi^2}{\partial \beta_\mu} \right|_{\Delta\beta_\mu} = 0 \qquad (\Delta\beta_\mu = \beta_\mu - \beta_{\mu_0})$$

To solve, we linearize

$$\left. \frac{\partial \chi^2}{\partial \beta_\mu} \right|_{\Delta\beta_\mu} = \left. \frac{\partial \chi^2}{\partial \beta_\mu} \right|_{\Delta\beta = 0} + \sum_\nu \frac{\partial^2 \chi^2}{\partial \beta_\mu \partial \beta_\nu} \Delta\beta_\nu = 0$$

Then, in analogy to eqn. A.3, the solution is

$$-y_\mu + \sum_\nu g_{\mu\nu} \Delta\beta_\nu = 0$$

$$\therefore \Delta\beta_\nu = \sum_\mu g^{-1}_{\mu\nu} y_\mu \qquad (A.9)$$

The new geometric constants therefore follow directly from eqns. A.6 and A.8, after a matrix inversion. Note that $g_{\mu\nu}^{-1}$ is the error matrix associated with these constants. With the exception of

$$\frac{\partial d_i^o}{\partial \beta_\mu}$$

all the quantities in $g_{\mu\nu}$ and y_μ are standard items found in all tracking algorithms based on least squares. The derivatives of d with respect to β are situation specific, which leads to the discussion of...

A.2 Application to the Mark II vertex detector

The strategy will be to modify the VC wire positions, effectively transforming the VC coordinates into the DC coordinate system. The β's parameterizing this transformation will be 3 infinitesimal rotations, and 2 linear offsets:

β_1 = rotation around x axis

β_2 = rotation around y axis

β_3 = rotation around z axis

β_4 = offset in x direction

β_5 = offset in y direction

Since the VC supplies no z information, the offset in the z direction is irrelevant.

Wire positions are specified by their location $\vec{W}$ and direction $\hat{W}$ at the center of the chamber (z=0). For small geometric displacements, $\hat{W}$ is approximately unchanged, and $\vec{W}$ transforms like

$$\begin{aligned} w_1' &= w_1 + \beta_3 w_2 - \beta_2 w_3 + \beta_4 \\ w_2' &= -\beta_3 w_1 + w_2 + \beta_1 w_3 + \beta_5 \\ w_3' &= \beta_2 w_1 - \beta_1 w_2 + w_3 \end{aligned} \qquad (A.10)$$

The question now is: what are the derivatives of the distance of closest approach with respect to the β's?

Consider, first, the calculation of the distance of closest approach. Let a track registering on wire ($\vec{W}$, $\hat{w}$) have position $\vec{P}$ and direction $\hat{t}$ at the point where it crosses that layer. A small mount of geometry shows that the DCA is given by

$$d_o = (\vec{W} - \vec{P}) \cdot \frac{\hat{w} \times \hat{t}}{|\hat{w} \times \hat{t}|}$$

In the VC, all wires are axial, so that $\hat{w} = \hat{k}$. Then

$$d_o = (\vec{W} - \vec{P}) \cdot \frac{-t_2 \hat{i} + t_1 \hat{j}}{\sqrt{t_1^2 + t_2^2}}$$

$$= \frac{-t_2 (W_1 - P_1) + t_1 (W_2 - P_2)}{\sqrt{t_1^2 + t_2^2}}$$

The derivative of the DCA is then given by

$$\frac{\partial d_o}{\partial \beta_\mu} = \frac{-t_2 \frac{\partial W_1}{\partial \beta_\mu} + t_1 \frac{\partial W_2}{\partial \beta_\mu}}{\sqrt{t_1^2 + t_2^2}}$$

The derivatives of W_1 and W_2 follow from eqns A.10, and the quantities

t_1 and t_2 are available in the tracking code. This completes the information required to find the β's via eqn A.9.

REFERENCES

1. M. L. Perl et al., Phys. Rev. Lett. 35, 1489 (1975).

2. J. Kirkby, in Proceedings of the 1979 Int. Symp. on Lepton Photon Interactions at High Energies, Batavia (1979).

3. Y. S. Tsai, SLAC-PUB-2450 (1979).

4. C. A. Blocker, Ph.D Thesis, LBL-10801 (1980).

5. D. H. Miller, Phys. Rev. D23, 1158 (1981).

6. T. W. Appelquist et al., Phys. Rev. D7, 2998 (1973).

7. F. J. Gilman and D. H. Miller, Phys. Rev. D17, 1846 (1978).

8. C. Matteuzzi et al., SLAC-PUB-3291 (1984).

9. K. G. Hayes et al., Phys. Rev., D25, 2869 (1982).

10. A. DeRujula, in Weak and Electromagnetic Interactions at High Energy, Les Houches, Session XXIX, 570 (1976).

11. X. Y. Lee and E. Ma, Phys. Rev. Lett. 47, 1788 (1981).

12. L. Abbott and E. Farhi, Phys. Lett. 101B, 69 (1981).
R. N. Mohapatra, CCNY-HEP-8216 (1982).

13. D. A. Bryman, Phys. Rev. Lett. 50, 7 (1983).

14. J. Jaros et al., Phys. Rev. Lett. 51, 955 (1983).

15. M. E. Levi, Ph.D. Thesis, Harvard University (1984).

16. C. A. Blocker et al., Phys. Rev. Lett. 49, 1369 (1982).

17. J. A. Jaros et al., Phys. Rev. Lett. 40, 1120 (1978).

18. R. H. Schindler, Ph.D. Thesis, SLAC-219 (1979).

19. G. S. Abrams et al., IEEE Trans., NS-25, 309 (1978).

20. G. S. Abrams et al., IEEE Trans., NS-27, 59 (1980).

21. J. D. Fox and M. E. B. Franklin, IEEE Trans., NS-28, 3 (1981).

22. J. M. Yelton et al., SLAC-PUB-3274 (1984).

23. N. S. Lockyer et al., Phys. Rev. Lett. 51, 1316 (1983).

24. C. S. Hoard, SLAC-TM-82-3 (1982).

25. Frodesen, Skjeggstad, and Tofte, Probability and Statistics in Particle Physics, Universitetsforlaget, Bergen (1979).

26. M. E. Nelson, Ph.D. Thesis, LBL-16724 (1983).

27. S. Weinberg, Phys. Rev. Lett. 19, 1264 (1967).

28. H. Fritzsch et al., Phys. Lett. 114B, 157 (1982).

29. G. H. Trilling, LBL Internal Memo, TG-360 (1982).

30. G. H. Trilling, LBL Internal Memo, TG-301 (1978).

TECHNICAL INFORMATION DEPARTMENT
LAWRENCE BERKELEY LABORATORY
UNIVERSITY OF CALIFORNIA
BERKELEY, CALIFORNIA 94720